Tropical Intraseasonal Variability Response to Zonally Asymmetric Forcing in an Idealized Moist GCM

CAMERON G. MACDONALD[a] AND YI MING[b]

[a] *Program in Atmospheric and Oceanic Sciences, Princeton University, Princeton, New Jersey*
[b] *NOAA/Geophysical Fluid Dynamics Laboratory, Princeton, New Jersey*

(Manuscript received 11 May 2022, in final form 14 July 2022)

ABSTRACT: The tropical intraseasonal variability in an idealized moist general circulation model (GCM) coupled to a slab ocean is investigated. The model has a simple moist convection scheme and realistic radiative transfer, but no parameterization of cloud processes. In a zonally symmetric aquaplanet state, variability is dominated by westward-propagating Rossby waves. Enforcing zonal asymmetry through the application of a prescribed ocean heat flux in the bottom boundary leads to the development of a slow, eastward propagating mode that bears some of the characteristics of the observed Madden–Julian oscillation (MJO). When the ocean heat flux is made stronger, high-frequency Kelvin waves exist alongside the MJO mode. The strength of the disturbances and the spatial distribution of their precipitation anomalies are sensitive to the strength of intraseasonal sea surface temperature (SST) anomalies. The greatest resemblance to the MJO is observed when shallow slab ocean depths (1 m) are used, but the mode still exists at deeper slabs. Sensitivity experiments to the parameters of the convection scheme suggest that the simulated MJO mode couples to convection in a way that is distinct from both Kelvin and Rossby waves generated by the model. Analysis of the column moist static energy (CMSE) budget of the MJO mode suggests that column radiative heating plays only a weak role in destabilizing the mode relative to the stabilizing contribution of vertical advection. The CMSE budget analysis highlights the importance of the life cycle of horizontal advection for the destabilization and propagation of the MJO. Synergies between the generated MJO mode and linear theories of the MJO are discussed as well.

KEYWORDS: Convection; Hydrologic cycle; Madden-Julian oscillation; General circulation models; Idealized models

1. Introduction

The Madden–Julian oscillation (MJO) is the strongest mode of intraseasonal variability observed over the Indo-Pacific warm pool (Madden and Julian 1971, 1972). Unlike other prominent modes of tropical wave variability such as Kelvin waves and equatorial Rossby waves, the MJO does not appear as a solution to the linear dry equations of Matsuno (1966). The wavenumber–frequency analysis of Wheeler and Kiladis (1999) further confirmed the MJO's existence as a distinct mode from convectively coupled equatorial Kelvin waves. This has led many to posit that atmospheric water vapor plays a key role in the dynamics of the MJO [see reviews by Zhang et al. (2020) and Jiang et al. (2020) for in-depth discussions of current theories of the MJO]. However, a consistent physical picture of the mechanisms that control the initiation, maintenance, and propagation of the MJO has yet to be attained in the 50 years since the identification of the phenomenon.

Moisture mode theories of the MJO (Adames and Maloney 2021) have provided promising insights into the dynamics of the MJO. The concept of a moisture mode, in which the presence of atmospheric water vapor is fundamental to the existence of equatorial wave modes, was defined in a formal manner by Sobel et al. (2001). Subsequent works (Fuchs and Raymond 2005, 2017) have incorporated surface heat exchange processes (Neelin et al. 1987; Emanuel 1987) into linear wave theories to evaluate their role in the destabilization of the MJO at planetary scales. Moisture mode theories (Sobel and Maloney 2012, 2013) have also described the dynamical fields of the MJO as being the response to the instantaneous localized heating of the MJO in the spirit of Gill (1980), with the localized heating determined by a prognostic moisture equation. Adames and Kim (2016) further developed this Gill-like response theory for the MJO. Subsequent work has suggested that moisture modes and the MJO may exist on a spectrum of tropical wave species (Adames et al. 2019).

In moisture mode theories of the MJO, the gross moist stability (GMS) (Raymond et al. 2009; Inoue and Back 2015b) plays an important role. The GMS measures the export of column moist static energy (CMSE) normalized by some measure of the strength of the large-scale circulation. Regions with negative GMS will increase their CMSE, while those with positive GMS will remove CMSE. Some moisture mode theories of the MJO rely on the reduction of the "effective" GMS felt by the column through diabatic effects such as cloud-radiative feedbacks (Adames and Kim 2016; Adames et al. 2019) to make the GMS negative and thus destabilize moisture modes. Conversely, Fuchs and Raymond (2017) showed that moisture modes may be destabilized at planetary scales by surface flux feedbacks in the absence of cloud-radiative effects, with the effective GMS remaining positive. Inoue and Back (2015b) and Inoue and Back (2017) showed that in reality, the GMS is a highly time-dependent quantity that fluctuates around a characteristic

---

Yi Ming's current affiliation: Schiller Insitute, Boston College, Boston, Massachusetts

---

Corresponding author: Cameron G. MacDonald, cgm3@princeton.edu

DOI: 10.1175/JCLI-D-22-0344.1

value, which is the relevant GMS quantity for the linear moisture mode instability.

The moisture mode framework is far from the only theoretical explanation that has been posited for the MJO. Recharge–discharge theories of the MJO (Bladé and Hartmann 1993; Hu and Randall 1994) suggest that the observed intraseasonal time scale of the MJO can be attributed to local convective processes associated with the recharge and discharge of column moist static energy. In this view, shallow vertical velocity profiles build up moist static energy within the column, which is then removed by the ensuing deep and then stratiform convection, leading to a period of weakened convection while the column starts to recharge its CMSE. Such theories require an explanation for the preferential development of shallow convection on the eastern margins of the MJO to explain its eastward propagation (Wolding and Maloney 2015). Benedict and Randall (2007) found that frictional moisture convergence in the boundary layer (Wang and Rui 1990; Maloney and Hartmann 1998) could act as a mechanism to initiate this convective life cycle.

The emergence of further theories in recent years highlights the challenges that still remain in understanding the MJO. Multiscale interaction theories (Majda and Stechmann 2009, 2011) suggest that the MJO is an envelope of smaller-scale convective features that interact nonlinearly with tropospheric water vapor. Quasi-equilibrium theories of the MJO hold some similarities to moisture mode theories and have variants that rely on cloud–radiation interactions to grow at planetary scales (Khairoutdinov and Emanuel 2018; Emanuel 2020) and those that are unstable without such feedbacks (Ahmed 2021). Recent work has shown these theories to be closely connected to certain moisture mode theories (Fuchs-Stone and Emanuel 2022). Gravity wave theories of the MJO (Yang and Ingersoll 2013, 2014) posit that the MJO is generated by interference between westward- and eastward-propagating gravity waves when convection is viewed as a triggered process. MJO theories rooted in the dry dynamics of the tropics have also been put forth; these theories (Wedi and Smolarkiewicz 2010; Yano and Tribbia 2017; Rostami and Zeitlin 2019) suggest that it is nonlinear Rossby wave dynamics, rather than tropospheric water vapor, that is essential to the presence of an MJO wave mode. While these theories have elicited varying degrees of attention in the scientific community, none of them is recognized as a complete explanation of the MJO.

In parallel with theoretical developments, idealized modeling studies of the MJO have attempted to elucidate its underlying physical mechanisms. The processes that destabilize and propagate the MJO in zonally symmetric settings have been explored in comprehensive GCMs with traditional convection parameterizations (Carlson and Caballero 2016), superparameterized convection (Andersen and Kuang 2012; Arnold et al. 2013; Arnold and Randall 2015), and with cloud-resolving resolution (Khairoutdinov and Emanuel 2018). Mechanism denial experiments (Kim et al. 2011; Andersen and Kuang 2012; Arnold and Randall 2015; Khairoutdinov and Emanuel 2018) have become common tools to assist in the identification of destabilization and propagation mechanisms for the MJO. Other studies have instead focused on the role that the Indo-Pacific warm pool plays in the existence of the MJO; Maloney et al. (2010) showed that a stronger MJO could be generated in fixed sea surface temperature (SST) simulations in which the SST distribution mimicked the observed pattern of Earth, relative to zonally symmetric simulations. However, the development of a strong MJO mode in Maloney et al. (2010) also relied on a reduction of the extratropical meridional SST gradient to a quarter of its observed value.

GCMs with simplified convection schemes have seen limited use in studying the MJO. In zonally symmetric configurations, models such as the one described in Frierson et al. (2006, 2007) when augmented with a simplified Betts–Miller convection scheme as in Frierson (2007b) have been shown to produce a robust band of Kelvin waves, but negligible MJO-like variability (Frierson 2007a). When enhanced with full-physics radiative transfer this model was shown to produce monsoon-like seasonal variability without any parameterizations of cloud processes (Clark et al. 2020).

In this study we run the idealized moist GCM of Clark et al. (2020) in an aquaplanet configuration with a slab ocean layer below. A zonally asymmetric state is induced via the application of a wavenumber-1 ocean heat flux to generate a warm pool in one hemisphere. This configuration will be shown to favor the generation of an MJO-like equatorial mode that produces slow eastward-propagating signals of precipitation and column water vapor in the warm pool sector. Composite analyses suggest that this mode is able to reproduce many of the equatorial and extratropical features of the MJO. The simple convection scheme used in the model allows for a more thorough understanding of how the MJO-like mode couples to moist convection.

The remainder of this paper is structured as follows: Section 2 describes the idealized moist GCM, experimental setups and analysis techniques used in the study. Section 3 describes the characteristics of the mean state and tropical variability of these simulations. Section 4 discusses the sensitivity of the tropical waves generated in the model to a few key parameters. Section 5 analyzes the column moist static energy budget of the MJO-like disturbances in the model, and discusses its connection to linear theories of the MJO. This is followed by a discussion and summary of results in section 6.

2. Methods

a. Model description

An idealized moist GCM is used to perform numerical experiments in this study. The modeling setup is built upon the idealized moist model of Frierson et al. (2006, 2007), with some modifications of parameterized physical processes as in Frierson (2007b) and Clark et al. (2018). The model has a spectral dynamical core that is run at T42 resolution, corresponding to 128 grid points in longitude and 64 grid points in latitude. The vertical structure of the model is that of Clark et al. (2020), with 40 unevenly spaced vertical levels. The bottom boundary of the model is a slab ocean with a uniform depth. The thermodynamic budget of this slab layer is

$$\rho_O c_{pO} d \frac{\partial T_s}{\partial t} = S - L - L_v E - H - \nabla \cdot \mathbf{F}_O, \qquad (1)$$

where ρ_O is the density of the layer, c_{pO} is its specific heat capacity, d is the depth of the mixed layer, and T_s is its temperature. Forcing terms are on the right-hand side, where S represents incoming shortwave radiation, L outgoing longwave radiation at the surface, L_vE latent heat fluxes, and H sensible heat fluxes. The final term on the right-hand side is the convergence of ocean heat fluxes. In this study, the ocean heat flux convergence will be prescribed to generate zonal asymmetry in the model.

Moist convection is parameterized as in Frierson (2007b) using a simplified Betts–Miller convection scheme (Betts and Miller 1986; Frierson 2007b). In this scheme temperature is relaxed back to a moist adiabat and water vapor is relaxed to a profile with constant relative humidity, consuming any positive convective available potential energy (CAPE) in the atmospheric column (Frierson 2007b). This formulation introduces two parameters into the model: a moist convective adjustment time scale τ_{SBM}, which controls how quickly temperature and moisture are returned to their reference profiles, and the relative humidity $\mathrm{RH}_{\mathrm{SBM}}$, which the moisture profile is relaxed back to. Previous studies have suggested that both the zonally averaged circulation (Frierson 2007b) and equatorial wave variability (Frierson 2007a) are sensitive to the values of these convection scheme parameters. Precipitation is instantly rained out when the criterion for convection or large-scale condensation (saturation at the grid scale) is satisfied, such that this model does not contain any clouds. The absence of clouds is an obvious departure from the real atmosphere; however, studying intraseasonal variability with this simple treatment of moist convection permits us to more easily manipulate the model and understand how convective motions couple to the large-scale circulation.

The changes introduced to the model by Clark et al. (2018) amount to adding a full-physics radiative transfer module to the model (Paynter and Ramaswamy 2014) to replace the gray-radiation scheme of Frierson et al. (2006, 2007), and using the planetary boundary layer scheme of O'Gorman and Schneider (2008). The use of the full-physics radiation allows for feedbacks between water vapor and radiation (Clark et al. 2018). The alternative boundary layer formulation is allowed to be unstable, in contrast to the original parameterization of Frierson et al. (2006, 2007), which could only be stable or neutral. This original scheme has been shown to support a robust spectrum of convectively coupled equatorial Kelvin waves (Frierson 2007a); we will show that a broader selection of equatorial waves can be simulated when the boundary layer is allowed to become unstable. The set of physical parameterizations as described is similar to those used in Merlis et al. (2013) and Jucker and Gerber (2017).

b. *Model experiments*

1) CORE MODEL EXPERIMENTS

Our control experiment consists of a zonally symmetric aquaplanet with a mixed layer depth of 1 m. This shallow depth is chosen as our control so that intraseasonal surface temperature variability has a reasonable magnitude in the absence of modulation of surface shortwave fluxes from clouds. The moist convective adjustment time is set to 2 h, following the suggestion of Betts and Miller (1986) and consistent with previous studies using similar modeling setups (Frierson 2007a,b; O'Gorman and Schneider 2008; Clark et al. 2018, 2020), and the relative humidity of the reference moisture profile is set to 70%. We run this experiment for 20 years in a perpetual equinox state, so there is no seasonal cycle. Analysis is performed on years 10–20 of the simulation. In this control setup with a shallow mixed layer, the model likely equilibrates much faster than the 9 years that are discarded (Clark et al. 2018); however, we choose this analysis period to ensure consistency with further sensitivity experiments that are run with deeper mixed layers.

To perturb the control experiment from its zonally symmetric state, we introduce a zonally asymmetric ocean heat flux divergence in the mixed layer ocean. The ocean heat flux pattern is sinusoidal in longitude with a wavenumber-1 pattern, and equatorially trapped with a Gaussian meridional profile using a RMS width of 18° in latitude. This pattern generates a corresponding wavenumber 1 pattern in the surface temperature of the mixed layer ocean to mimic, in an idealized sense, the Indo-Pacific warm pool present on Earth. In our case the cold-pool region resides in the Eastern Hemisphere (0°–180°) and the warm pool in the Western Hemisphere (180°–360°). In using a sinusoidal pattern for the ocean heat flux divergence, no additional energy is added into the system through the bottom boundary in the global average. We run three different zonally asymmetric experiments with the amplitude of the ocean heat flux set to 25, 50, and 100 W m^{-2}. These three amplitudes correspond to equatorial temperature contrasts of about 2, 5, and 10 K, respectively. Throughout the rest of the paper, these three experiments will be referred to as Q25, Q50, and Q100.

2) SENSITIVITY EXPERIMENTS

We run a number of additional experiments to explore the sensitivity of equatorial wave variability to some key parameters in the model in the asymmetric state. First, we run experiments with different depths of the ocean mixed layer. Using the Q50 case as a starting point, we perform model runs with the mixed layer depth of the ocean set to 0.1, 20, and 100 m.

We also run experiments similar to that of Frierson (2007a) to test the sensitivity of the model to the parameters of the convection scheme. Again using the Q50 run as the base point about which we perturb the model, we perform two additional experiments where the relative humidity of the reference moisture profile ($\mathrm{RH}_{\mathrm{SBM}}$) is varied: one where we decrease $\mathrm{RH}_{\mathrm{SBM}}$ to 60% and another where it is increased to 80% compared to its control value of 70%. One additional test of the sensitivity to the convection scheme is performed by increasing the moist convective adjustment time τ_{SBM} to 16 h from its initial value of 2 h. This is the point at which Frierson (2007b) observed a transition in the strength of the zonally averaged precipitation in the tropics in his zonally symmetric experiments.

c. *Analysis techniques*

1) SPACE–TIME SPECTRAL ANALYSIS

The main interest of this study is the tropical wave variability of the equatorial belt. To further elucidate the behavior of these waves, we transform various fields into their space–time spectral representations to isolate modes at specific wavenumbers and frequencies. We employ the fast Fourier transform (FFT) method of Welch (1967) as described by Wheeler and Kiladis (1999). The time series of a variable is split into a series of 192-day segments that overlap by 96 days, and a Hanning window is applied to taper the ends of the segments. The FFT is then applied to the time and longitude coordinates, and the resulting spectral representation is averaged over each segment and each latitude from 10°S to 10°N weighted by the surface area of the grid cells at each latitude. A red spectrum is computed by applying a 1–2–1 filter 40 times along the frequency dimension and 10 times along the wavenumber dimension. Finally we calculate the signal strength S at each wavenumber and frequency as in Clark et al. (2020) by

$$S = \frac{P - R}{P}, \tag{2}$$

where P is the power spectrum and R is the red spectrum.

To determine the statistical significance of the signal strength, we employ a chi-squared test at the 99% level. Wheeler and Kiladis (1999) calculate the number of degrees of freedom for the normalized power P/R as

$$n = \frac{2\,(\text{amplitude and phase}) \times 11\,(\text{years}) \times 8\,(\text{latitudes}) \times 365}{192\,(\text{segment length})} \approx 335, \tag{3}$$

so that the critical value of the normalized power is $(P/R)_c = \chi_c^2/(n-1) = 1.19$, where χ_c^2 is the value of the chi-squared cumulative distribution function at its 99th percentile. Transforming this critical normalized power into a critical signal strength as in Clark et al. (2020), we find that the criterion for significance is $S > 0.16$.

2) Lagged regression analysis

Lagged regression analysis is used to construct composite tropical disturbances out of the model time series. Indices for the regressions are calculated by spectrally filtering equatorial precipitation anomalies to retain only the variability associated with the spectral region of the waves of interest. This index is then standardized by removing its time mean and normalizing by its standard deviation, providing a nondimensional vector $\hat{\mathbf{P}}$, against which we can regress any variables output from the model (Adames and Wallace 2014a; Adames and Kim 2016; Clark et al. 2020). Specifically, regression maps are calculated as

$$\mathbf{D} = \frac{\mathbf{S}\hat{\mathbf{P}}^{\mathrm{T}}}{N}, \tag{4}$$

where the rows of the matrix $\mathbf{S}$ contain the time series of the regressed variable at each grid cell (and vertical level for three-dimensional fields), and N is the number of entries in the time series. By shifting the index in time, we can calculate regression maps lagging or leading the index and view the time evolution of the composite event.

The statistical significance of the regression coefficients contained in $\mathbf{D}$ are evaluated using a two-tailed Student's t test at the 99% significance level, with the number of degrees of freedom equal to the number of entries in the time series. From this test, regression values are considered significant if the correlation coefficient of the regression is greater than 0.02. Multiplying by the standard deviation of the time series in question then gives a critical magnitude for the regression coefficient above which results are considered statistically significant.

3) Velocity potential indices for intraseasonal oscillations

We also utilize the principal component analysis (PCA) techniques described in Adames and Wallace (2014a). The PCA is performed on the velocity potential difference ($\Delta\chi$) between the 850- and 150-hPa levels. As described in Adames and Wallace (2014a), since the velocity potential is the inverse Laplacian of the divergence field, it captures primarily convergence that occurs on the planetary scale. Upper-level divergence (convergence) and lower-level convergence (divergence) will then be associated with positive (negative) values of $\Delta\chi$. Adames and Wallace (2014a) showed that this velocity potential index performs similarly to other MJO indices, including the real-time multivariate (RMM) MJO index of Wheeler and Hendon (2004). The RMM index uses outgoing longwave radiation (OLR) as one of its predictors; in our cloud-free model OLR may have different characteristics from those of Earth and so we prefer the velocity potential index, which relies only on dynamical fields. Straub (2013) showed that the dynamical fields supplied to the RMM index are more important relative to the OLR. In atmospheres that support propagating intraseasonal oscillations, such as the MJO on Earth, the resulting first two empirical orthogonal functions (EOFs) yield wavenumber-1 patterns that are in quadrature with one another. An index for any phase α of the MJO can then be constructed using the principal components (PCs) of EOF1 and EOF2:

$$\hat{P}(t) = \mathrm{PC}_1(t)\cos\alpha + \mathrm{PC}_2(t)\sin\alpha, \tag{5}$$

where PC_1 and PC_2 are the PCs corresponding to EOF1 and EOF2, respectively. Regressions of the form of Eq. (4) can then be carried out using these indices. Under this convention and using the same sign conventions for EOF1 and EOF2 as Adames and Wallace (2014a), $\alpha = 0°$ and $\alpha = -90°$, would correspond to an active MJO over the Maritime Continent and the Indian Ocean, respectively. In our asymmetric experiments, these phases correspond to an active MJO over the center of the warm pool (270°E) and the western region of the warm pool (180°), respectively.

To construct summaries of a composite ISO over its active phase, we use the "warm-pool compositing" technique described in Adames and Wallace (2014b, 2015). Regression maps at equally spaced intervals (1/32 of the MJO phase) are averaged after shifting the maps in longitude so that their respective maxima of $\Delta\chi$ are located at the same reference longitude. As in Adames (2017), this summary map will be referred to as warm pool composite 1 (WPC1). We could formally write this composite as

$$\mathrm{WPC1}(\mathbf{D}) = \frac{1}{\pi}\int_{-\pi/2}^{\pi/2} \mathbf{D}[\alpha, \lambda + \lambda_{r1}(\alpha), \varphi, p]\,d\alpha, \qquad (6)$$

where $\lambda_{r1}(\alpha)$ is the longitude at which $\Delta\chi$ reaches it maximum. Significance criteria for the warm pool composites are treated in a similar manner to the lagged regression analysis.

3. Results

a. Mean state response to asymmetric forcing

We first examine how the addition of the zonally asymmetric ocean heat flux influences the time-mean and zonal-mean state of the climate. Figure 1a shows the meridional distribution of the zonally averaged surface temperature for the control run and the Q25, Q50, and Q100 experiments. The temperature distributions in the midlatitudes remain similar between experiments. At the equator, the meridional gradient of the surface temperature is reduced as the amplitude of the forcing is increased, such that the bump that is observed at the equator in the control run has been completely smoothed out in the Q100 run. Frierson (2007b) observed a similar bump when changes were made to the convection scheme of their zonally symmetric model.

Figure 1b shows the zonal distribution of surface temperatures at the equator. It should be noted that since the model is run on a Gaussian grid, "equatorial" values are actually the average of the two grid cells whose boundary lies on the equator. The inclusion of the ocean heat flux cools the surface temperatures of the Eastern Hemisphere and warms those of the Western Hemisphere. Since the zonal-mean surface temperature decreases as the forcing is increased, we see that the tropics of the cold hemispheres are colder relative to the control run than the tropics of the warm hemispheres are warm. This is due to an increase in zonal mean surface latent heat flux at the equator with increased asymmetry (not shown).

Figure 1c shows the total meridional moist static energy (MSE) transport and its decomposition into transport of dry static energy (DSE) and moisture. While the total MSE transport (solid lines) remains largely the same in the tropics with varied asymmetric forcing, the magnitudes of the DSE transport (dashed lines) and moisture transport (dash-dotted lines) reduce as the strength of the asymmetric forcing is increased in such a way that their sum remains virtually unchanged. The contributions of DSE and moisture in the extratropics are qualitatively unaffected by the addition of the asymmetric forcing until the Q100 case, when DSE (moisture) transport increases (decreases) slightly.

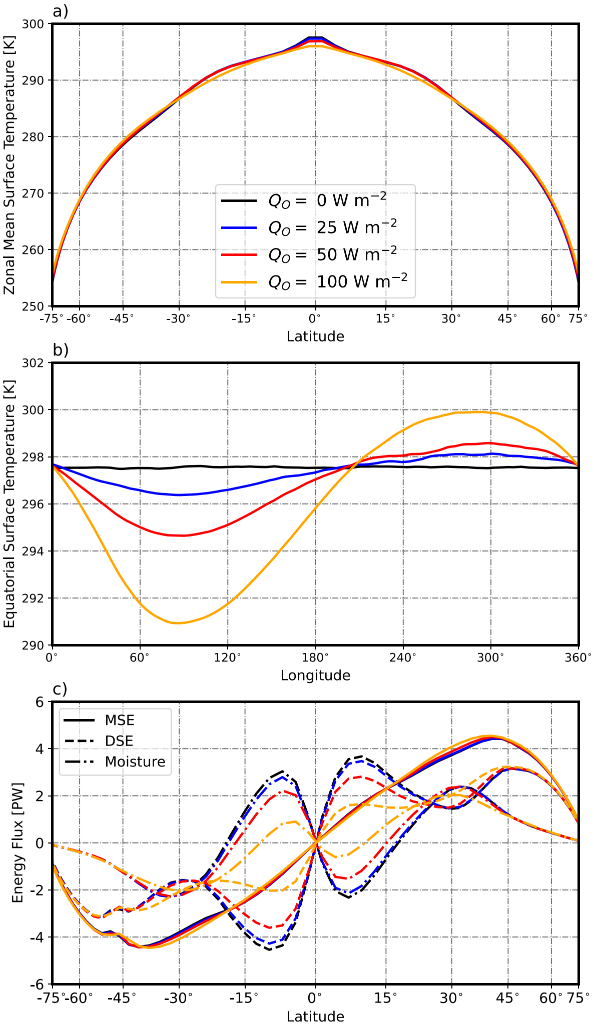

FIG. 1. (a) Meridional distribution of the zonally averaged surface temperature for the control run and the Q25, Q50, and Q100 experiments. The meridional axis scales with the sine of latitude to accentuate the tropical belt. (b) Zonal distribution of surface temperatures at the equator for the control run and the three zonally asymmetric experiments. (c) Total meridional energy flux (solid lines) and its decomposition into its contributions from dry static energy (dashed lines) and moisture (dash-dotted lines) for each experiment.

The zonally asymmetric ocean heat flux has profound effects on the zonal mean circulation of the atmosphere. Figure 2 shows the meridional overturning circulation and zonal-mean zonal winds for each run. In the control run (Fig. 2a) the standard equinoctial Hadley cell (HC) and westerly subtropical jets (STJs) are produced in each hemisphere. As the forcing is increased, the tropical upper troposphere develops westerly winds and begins to superrotate: in the Q25 run (Fig. 2b), this superrotation is weak, and the zonal-mean zonal winds are similar to the control run. When the strength of the forcing is doubled in the Q50 run (Fig. 2c) the superrotation has strengthened so that the upper tropospheric zonal winds are on the order of 10 m s^{-1}, and the strength of the STJs has weakened considerably. In the Q100 run (Fig. 2d), a westerly jet forms at the equator and the STJs have moved slightly equatorward. The zonal distribution of upper tropospheric winds (not shown) reveal that the superrotation is driven by strong westerly winds in the cold hemisphere, where the STJs have been eliminated such that the upper tropospheric dynamical fields form a coupled Kelvin–Rossby (KR) pattern (Showman and Polvani 2011).

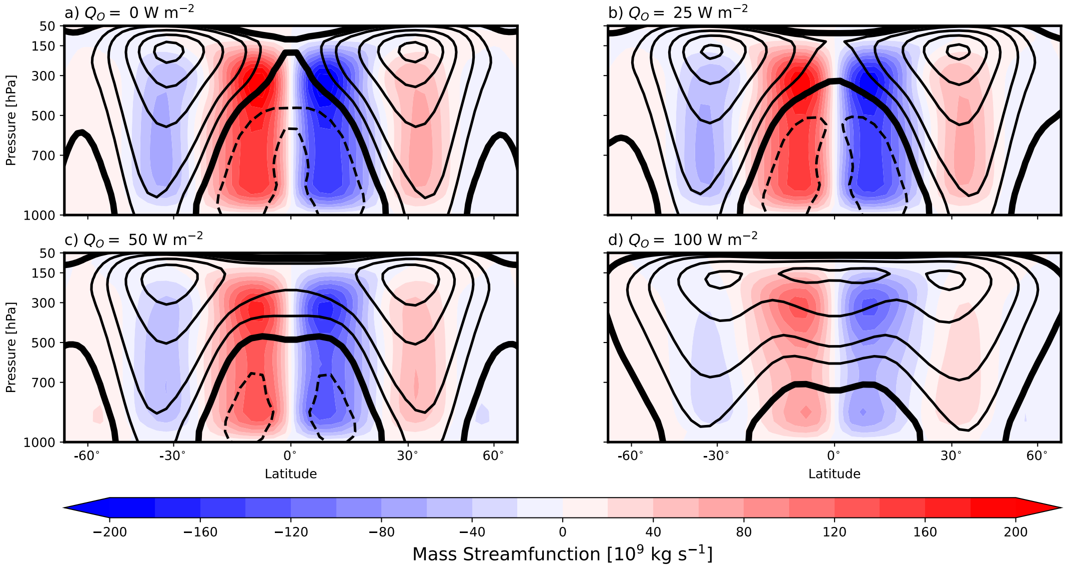

FIG. 2. Eulerian mass streamfunction (shading) and zonal mean zonal wind (black contours) for the (a) control run, (b) Q25 run, (c) Q50 run, and (d) Q100 run. The thick black contour shows the zero line of zonal mean zonal wind, and the contour interval is 10 m s^{-1}, with additional contours added at the −5 and +5 m s^{-1} levels.

The development of superrotation as a result of asymmetric forcing is consistent with previous studies using both two-layer models (Suarez and Duffy 1992; Saravanan 1993) and dry multilevel GCMs (Kraucunas and Hartmann 2005; Lutsko 2018).

The strength of the HC is also affected by the asymmetric forcing. The overturning streamfunction for the Q100 case shown in Fig. 2d is about half the strength of the control run (Fig. 2a). This transition to a weaker HC occurs rather abruptly between the Q50 and Q100 runs, whereas the transition to equatorial superrotation occurs smoothly as the asymmetric forcing is increased. Kraucunas and Hartmann (2005) also saw a reduction in the strength of the HC after imposing a zonal wavenumber-2 heating distribution in their dry multilevel GCM.

Figure 3 shows the distributions of time mean precipitation and column saturation fraction (Bretherton et al. 2004; Adames 2017), defined as $\langle\overline{q}\rangle/\langle\overline{q_s}\rangle$, where q is the specific humidity, q_s is the saturation specific humidity, the overbar indicates a

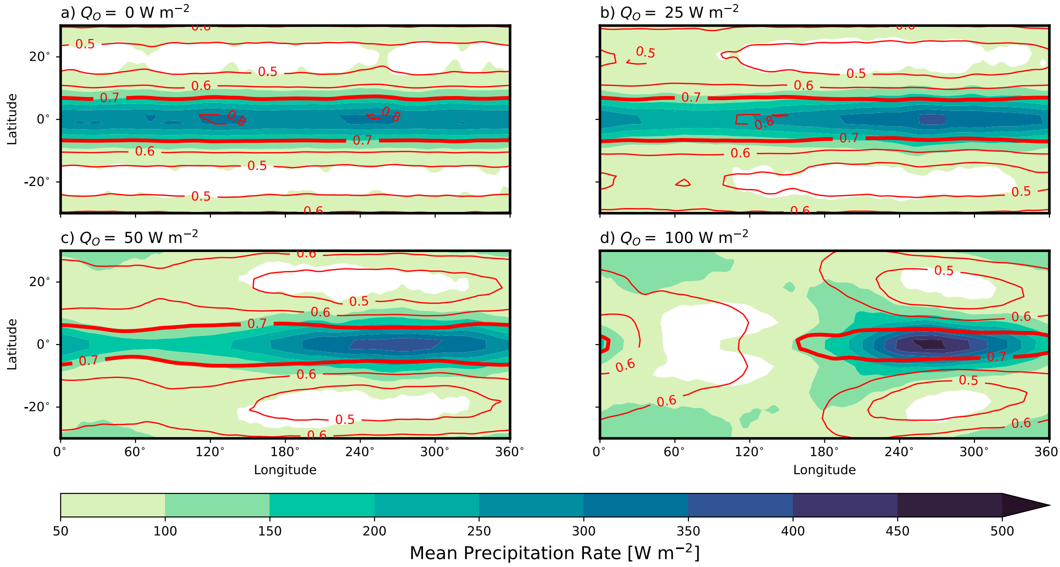

FIG. 3. Time-mean precipitation (shading) and column saturation fraction (red contours) for the (a) control run, (b) Q25 run, (c) Q50 run, and (d) Q100 run. The thick contour shows the simplified Betts–Miller relative humidity used in the convection scheme.

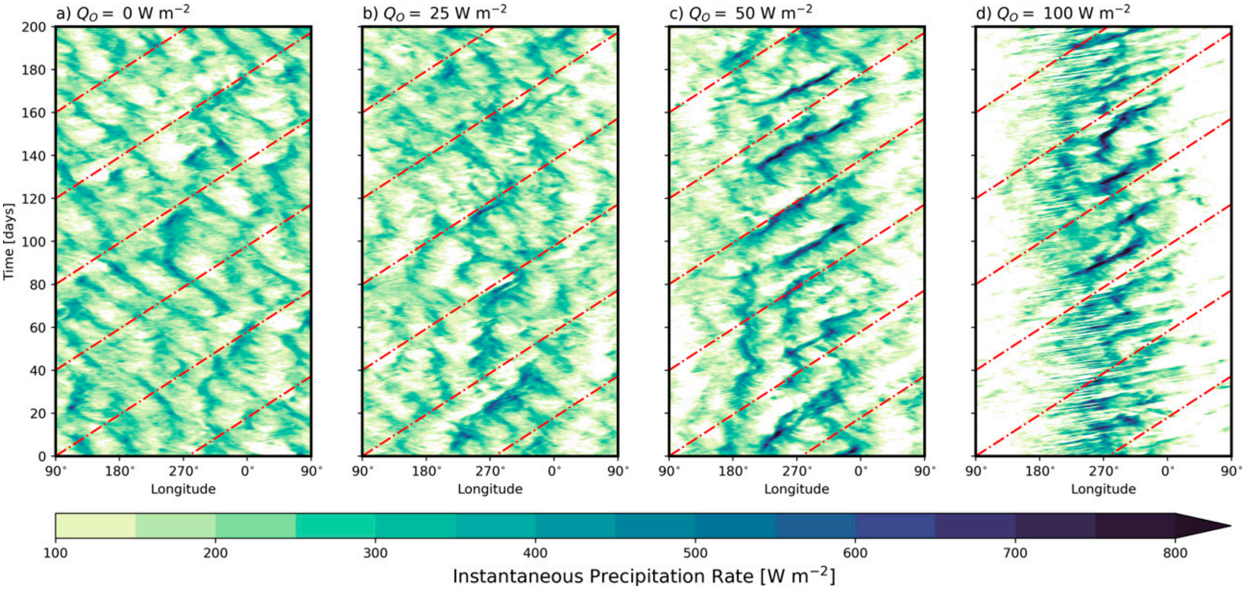

FIG. 4. Hovmöller plots of precipitation for the (a) control run, (b) Q25 run, (c) Q50 run, and (d) Q100 run, with shading showing instantaneous precipitation averaged from 10°S to 10°N for 200-day segments of the model runs. Red dash-dotted lines show lines of 6 m s^{-1} eastward phase speed, which is about the speed the simulated MJO disturbances travel across the warm pool. The images have been shifted in longitude so that the warm pool lies at the center of the frame.

time mean, and the angle brackets indicate a pressure integral from the surface to 100 hPa. In the control, Q25, and Q50 experiments (Figs. 3a–c), mean precipitation can be well described as a function of the column saturation fraction; the drying of the tropics in the cold hemisphere and the subtropics in the warm hemisphere are captured in both fields. Furthermore, in these three experiments the climatologically wet regions ($\overline{P} > 100\,\mathrm{W\,m^{-2}} \approx 3.6\,\mathrm{mm\,day^{-1}}$) are enclosed in the regions of the tropics where the column saturation fraction exceeds the relative humidity of the reference moisture profile of the model's convection scheme $\mathrm{RH_{SBM}}$ (the thick red contour in Fig. 3). In all three cases this wet region extends across the entire tropical belt.

The Q100 case (Fig. 3d) departs significantly from the control run. The cold hemisphere now contains a large dry region in the tropics with mean precipitation less than 50 W m^{-2}, while the subtropics of this hemisphere have become much wetter. Along with the strong mean precipitation of the tropics in the warm hemisphere, this lends a wavenumber-1 KR pattern to the mean precipitation. There is also less coherence between the precipitation and column saturation fraction; in the western portion of the warm pool there are wet regions that reside outside the region in which $\langle\overline{q}\rangle/\langle\overline{q_s}\rangle > \mathrm{RH_{SBM}}$.

b. Tropical variability response

We now investigate the response of tropical wave activity to asymmetric forcing. Figure 4 shows Hovmöller plots of equatorial precipitation averaged over 10°S–10°N for 200-day segments in each experiment. For the control run shown in Fig. 4a, the dominant mode of variability is westward-propagating Rossby waves, which exist throughout the entirety of the domain. Upon the addition of the asymmetric forcing in the Q25 case (Fig. 4b), a new mode of intraseasonal tropical variability emerges alongside the Rossby waves. These waves propagate eastward with a phase speed of around 6 m s^{-1} (shown by the red dash-dotted lines in Fig. 4) and are active only over the warm pool sector. These are both fundamental characteristics of the observed MJO on Earth, although the simulated MJO-like variability has a shorter period (~30 days) relative to the observed MJO (40–50 days).

Upon a further increase in the strength of the asymmetric forcing in the Q50 case (Fig. 4c), these eastward-propagating waves clearly become the dominant mode of tropical variability. Whereas in the Q25 case these intraseasonal oscillations seemed to be isolated events, in the Q50 case we see multiple MJO-like events occurring successively between days 80 and 160 of the time series. The Q50 case also exhibits states of convective self-aggregation; for the first 80 days of the time series, a stationary region of precipitation exists on the western edge of the warm pool around 180°E before it eventually appears to trigger an MJO-like event around day 80.

Figure 4d shows a Hovmöller plot for the Q100 case. Here we see another transition on the behavior of tropical waves. The first 80 days of the time series are dominated by high-frequency Kelvin wave activity over the warm pool sector, while days 80–160 contain a series of strong, successive MJO-like events before gradually returning to a Kelvin wave–dominated regime for the final 40 days. Interestingly, these two regimes appear to be mutually exclusive: the Kelvin wave activity vanishes from the tropical belt when the MJO is active and vice versa. This is in contrast to observational analysis such as that of Wheeler and Kiladis (1999), which suggests that an active MJO may coexist with Kelvin waves (cf. their Fig. 9). In this strongest

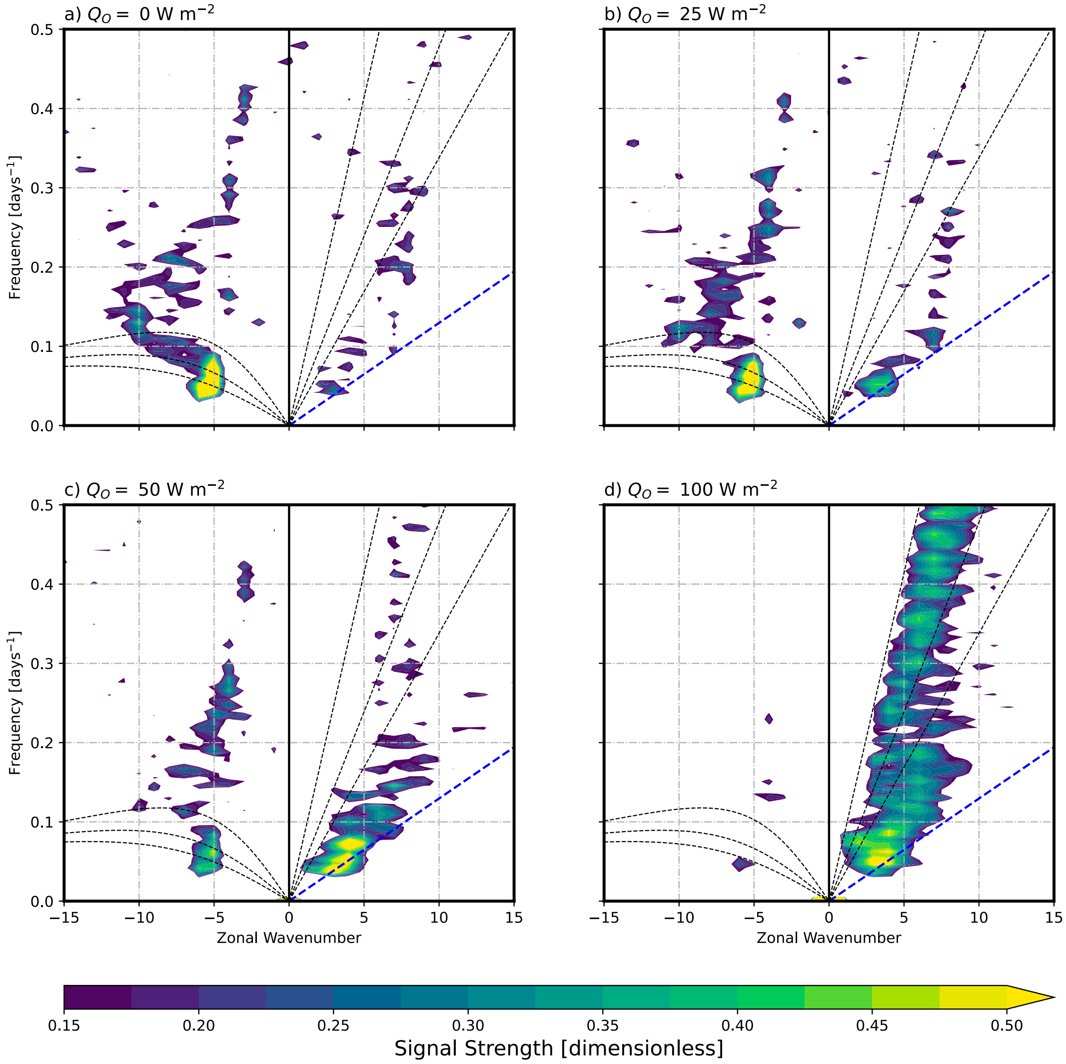

FIG. 5. Space–time power spectra of equatorial precipitation for the (a) control run, (b) Q25 run, (c) Q50 run, and (d) Q100 run. Shading shows the normalized signal strength of precipitation averaged from 10°S to 10°N. Dashed black lines show dispersion curves for Kelvin and $n = 1$ equatorial Rossby waves with equivalent depths of 25, 50, and 150 m. The thick blue dashed line shows the 6 m s^{-1} phase speed line. Only values that pass a chi-squared significance test are shaded.

forcing case, virtually all precipitation variability has been eliminated from the cold pool sector.

We next transform these equatorial precipitation time series into their signal strength in spectral space using the method described in section 2c(1). Since we choose to segment the times series into 192-day periods, the Hovmöller plots in Fig. 4 are representative of each segment. Figure 5a shows the signal strength of precipitation for the control run. Consistent with the Hovmöller plot, the strongest signal comes from Rossby waves at zonal wavenumber $k = -5$. There is some spurious eastward propagating signal at intraseasonal time scales and in the Kelvin wave band. For the Q25 case (Fig. 5b) a stronger MJO signal is observed between $k = 2$ and $k = 5$. This signal falls approximately along the 6 m s^{-1} phase speed line (the thick blue dashed line in Fig. 5). Moving to the Q50 case in Fig. 5c, the MJO spectral region overtakes the Rossby waves as the mode with the strongest signal. In the Q100 case (Fig. 5d), high-frequency Kelvin wave activity now appears as a large source of variability, while essentially all of the westward-propagating disturbances have been eliminated. The Kelvin wave variability lies between the 50- and 150-m equivalent depth dispersion curves, so these waves travel faster than observed convectively coupled Kelvin waves on Earth, which have an equivalent depth of 25 m (Wheeler and Kiladis 1999). Frierson (2007a) also found that Kelvin waves propagated faster than observed in the gray-radiation equivalent of this model. Once again the strongest signal appears along the 6 m s^{-1} phase speed line, indicating that MJO-like variability is a robust feature of all the asymmetric experiments.

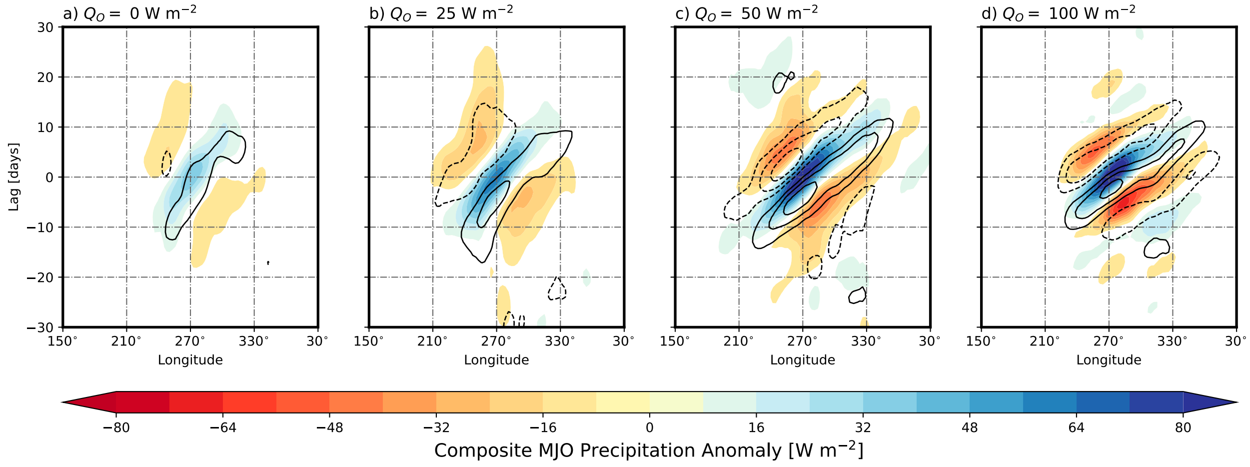

FIG. 6. Lagged time series from −30 to +30 days of a composite MJO for the (a) control run, (b) Q25 run, (c) Q50 run, and (d) Q100 run. Shading shows precipitation anomalies averaged between 10°S and 10°N, and the contours show intraseasonal SST anomalies. The contour interval is 0.1 K, with negative contours dashed and the zero contour omitted. Values that do not pass a two-sided t test for significance are masked in white. Images have been shifted such that the warm pool lies at the center of the frame.

To view the time evolution of the MJO mode generated by the model, we use lag regression analysis as described in section 2c(2). As an index we use equatorial precipitation filtered to include variability only on intraseasonal time scales (10–100 days) and eastward planetary scales (zonal wavenumbers 1–10) and averaged over the region 265°–275°E, 10°S–10°N. The lower bound of the intraseasonal frequency range has been decreased to 10 days from the more common bound of 20 days as this was found to better capture precipitation anomalies in Hovmöller plots (not shown). Precipitation and SST are then regressed against this index for lags ranging from −30 to +30 days. The resulting lagged time series for the control run and the zonally asymmetric experiments are shown in Fig. 6. The strength of the composite precipitation anomalies increases considerably from the control run to the Q25 run. In all cases, SST anomalies lead the MJO precipitation anomalies by about 4 days. In the Q50 case, in which the strongest MJO-like variability was observed, the strongest intraseasonal SST anomalies are on the order of 0.3 K. Studies with slab oceans coupled to comprehensive GCMs (Waliser et al. 1999; Maloney and Sobel 2004) generally require far deeper slabs than the 1-m depth used here to produce the same magnitude of SST variations. Due to the absence of clouds in our model, the intraseasonal shortwave radiative flux at the surface is modulated only through water vapor–radiation interactions. This produces a much weaker effect than is observed for Earth; the shallow mixed layer (ML) depth allows intraseasonal SST variations with the correct magnitude and phase relationship with precipitation.

A robust feature across all the lagged time series in Fig. 6 is the apparent westward group velocity of the simulated MJO. This can be seen by tracking the location of the consecutive peaks and troughs in precipitation: the dry phase that follows the convectively active phase of the MJO occurs significantly farther west than the preceding dry phase. Adames and Kim (2016) observed a similar westward group velocity in regressions of reanalysis data onto a MJO-filtered index of outgoing longwave radiation (OLR). Chen and Wang (2018) argued that the westward group velocity reported in Adames and Kim (2016) was a result of the spectral filtering used in that study, which filtered out sub-planetary-scale effects related to the transit of the MJO across the Maritime Continent (MC). However, our aquaplanet model produces an apparent westward movement of precipitation maxima without the presence of the MC.

c. *Three-dimensional structure of the simulated MJO*

We employ the EOF-based regressions described in section 2c(3) to investigate the three-dimensional structures of the intraseasonal disturbances that are prominent in the warm pool sectors of the three asymmetric simulations. Figure 7a shows WPC1 of precipitation and midtropospheric pressure velocity for the Q25 run. This case exhibits characteristics associated with the MJO in previous studies of reanalysis products (Adames and Wallace 2014b, 2015; Adames 2017). Most notable is the swallow-tail shape of the main precipitation anomaly, with an equatorially trapped signal leading the reference longitude and two lagging off-equator anomalies at around 10°N/S. The magnitude of the precipitation anomalies is similar to those found in Adames and Wallace (2015) using observed precipitation. The pressure velocity has a similar swallow-tail shape. These figures also highlight the extratropical interactions of the simulated MJO: regions of anomalously high precipitation and ascent are located at 30°N/S around 60° ahead of the convective center of the disturbance, and regions anomalously low precipitation and subsidence about 150° ahead of the disturbance.

Figure 7b shows the same composited fields for the Q50 case. The zonal extent of the main precipitation disturbance has decreased, but the striking resemblance to the observed MJO is retained; disparities with the equivalent reanalysis-based composites in Adames (2017) can in part be attributed to the northward

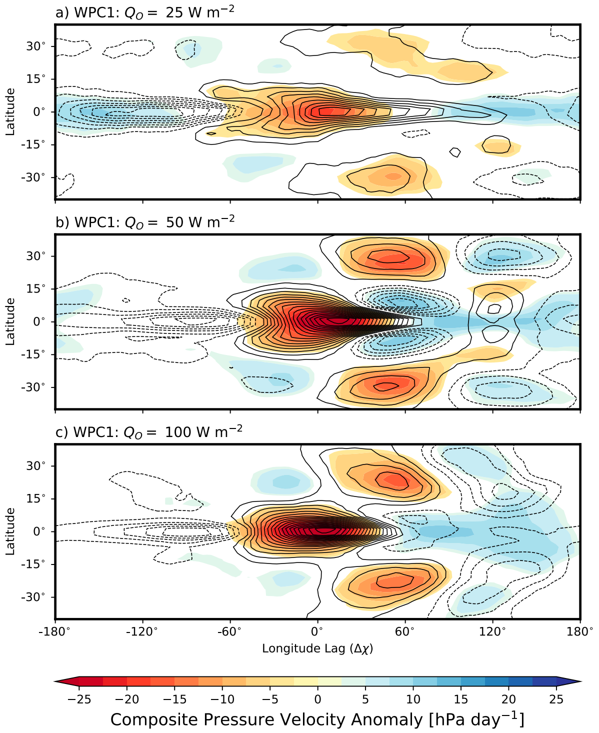

FIG. 7. WPC1 of precipitation (contours) and 400-hPa pressure velocity (shading) anomalies for the (a) Q25 run, (b) Q50 run, and (c) Q100 run. The contour interval for precipitation is 3 W m^{-2}, with negative values dashed and the zero contour omitted. Values that do not pass the statistical significance test are masked with white.

displacement of the intertropical convergence zone (ITCZ) on Earth over the eastern Pacific, whereas in our model the ITCZ lies on the equator across the entire tropical belt. Additionally, the extratropical regions of ascent and descent are considerably stronger than in the Q25 run. Further meridional WPC cross sections (not shown) suggest that the extratropical "flanking Rossby waves" identified by Adames and Wallace (2014a) are reproduced in our model in the Q25 and Q50 runs. WPC1 for the Q100 run is shown in Fig. 7c. Here some of the resemblance to the observed MJO has been lost, as the precipitation field exhibits less of a swallow-tail shape than in the previous two runs, and the disturbance has become more closely trapped to the equator, giving the disturbance more of a Kelvin wave–like disposition. The extratropical features however retain their previous structure, and are of a similar strength to those observed in the Q50 case.

We now look at the anomalous moisture and overturning circulation of the simulated MJO events in the equatorial plane. Figure 8 shows MJO-related anomalies of RH, specific humidity, and zonal circulation. For the Q25 case (Fig. 8a), WPC1 gives a roughly zonal wavenumber-1 pattern in the moisture fields. Specific humidity anomalies are confined below around 300 hPa, while relative humidity anomalies extend through the upper troposphere to above 100 hPa. Both fields exhibit a westward tilt with height, with positive boundary layer specific humidity anomalies extending more than 120° ahead of the reference longitude, but midtropospheric anomalies are more confined to the convective center of the MJO. RH anomalies have a similar westward tilt throughout the depth of the troposphere, but then take on an opposite, eastward tilt with height near the tropopause, similar to the structure found for the MJO-related RH in Adames and Wallace (2015). The zonal circulation has a double overturning cell pattern, and produces a single large subsidence region away from the convective center of the MJO.

The magnitude of the RH anomalies at the center of the MJO increases considerably in the Q50 run (Fig. 8b). The westward tilts of the moisture fields have also been reduced; lower-tropospheric specific humidity anomalies are now confined primarily to within 60° of the reference longitude, and upper-tropospheric RH anomalies lie roughly over top of the lower-tropospheric anomalies. The overturning circulation has become more complex. There is now a region of subsidence around 60° ahead of the reference longitude, associated with the leading overturning cell of the MJO that is now separate from the subsidence of the lagging overturning cell. This appears to assist in shallowing the positive specific humidity anomalies leading the region of deep convection.

In the Q100 case (Fig. 8c), the maximum positive RH anomaly has now decreased relative to the Q50 case, perhaps due to the more Kelvin wave–like structure of the wave. The positive specific humidity anomalies have been further confined to the convective center of the MJO. The main subsidence region is now associated with the lagging overturning cell of the zonal circulation, however this region has shifted farther westward such that it resides closer to the leading edge of the MJO. This results in strong negative specific humidity anomalies in the lower troposphere between 60° and 180° ahead of the reference longitude, and negative RH anomalies in the upper troposphere that are larger in magnitude than the positive anomalies at reference longitude.

d. *Vertical structures of the vertical velocity*

Reanalysis studies of the MJO suggest that the vertical structure of the vertical velocity is dominated by a first baroclinic mode, with ascent throughout the depth of the troposphere that maximizes at a midtropospheric level around 400 hPa (Adames and Wallace 2014b, 2015). The residual structure of the vertical velocity largely takes on a second baroclinic mode with opposing motion in the lower and upper troposphere, corresponding to either shallow or stratiform convection. Shallow convection is observed leading the center of the MJO and stratiform convection trailing it, lending the divergence field of the MJO its characteristic westward tilt with height (Adames and Wallace 2014b; Zhang et al. 2020). We use the PCA method described in Adames and Wallace (2014b) to decompose the three-dimensional regression map of the MJO vertical velocity field into a series of vertical modes and horizontal maps as

$$\omega(x, y, p) = \sum_{k=1}^{N_\ell} \omega_k(x, y)\Lambda_\omega^{(k)}(p), \tag{7}$$

where ω_k are a set of horizontal maps that describe the modal structure of the vertical velocity, $\Lambda_\omega^{(k)}$ are their corresponding

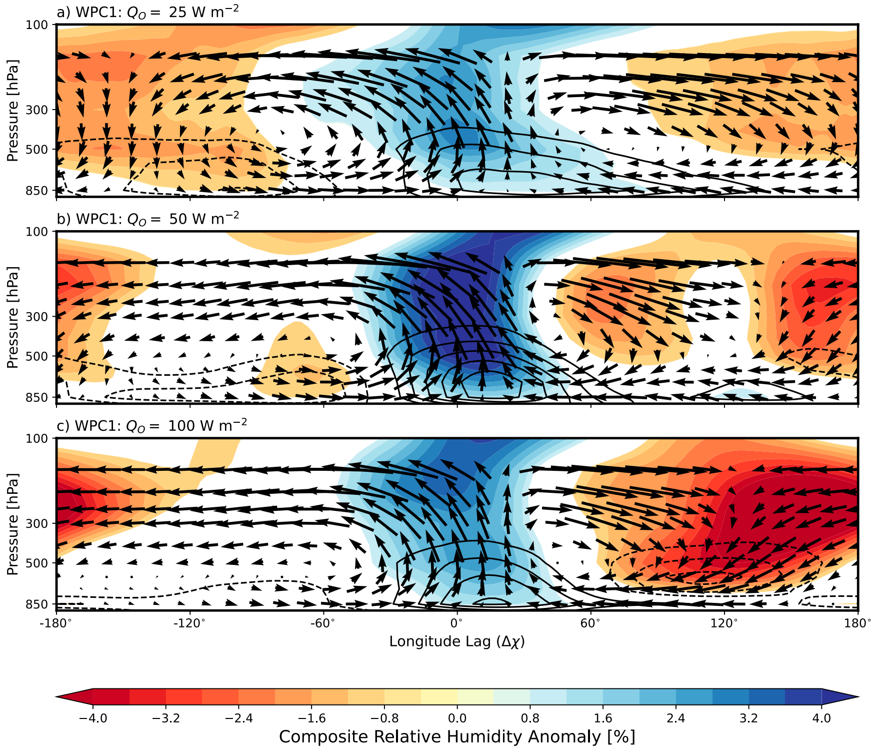

FIG. 8. WPC1 of RH (shading), specific humidity (contours), and equatorial overturning circulation [(u,ω) vectors] anomalies for the (a) Q25 run, (b) Q50 run, and (c) Q100 run. The contour interval for the specific humidity is 0.04 g kg^{-1}, and the zero contour is omitted. The ω values for the vectors have been scaled by -10^2 to improve visualization and have upward arrows correspond to ascending motion. Values that do not pass the statistical significance test are masked with white.

vertical structures, and N_ℓ is the number of vertical levels. The term $\Lambda_\omega^{(1)}$ then corresponds to the deep convective mode, and $\Lambda_\omega^{(2)}$ to the shallow or stratiform mode depending on the sign of the horizontal map; more complex vertical structures will be represented by the remaining terms of the expansion.

The contours in Fig. 9 show WPC1 of the first baroclinic mode of the vertical velocity filtered to intraseasonal time scales for the Q25, Q50, and Q100 experiments. For the Q25 experiment (Fig. 9a) the ascent region occupies about 120° of longitude, with maximum ascent occurring directly over the reference longitude at around 400 hPa. The anomalous subsidence region occupies the rest of the equatorial plane, with maximum descent trailing the convective center of the MJO mode. For the Q50 experiment (Fig. 9b), the ascent region of the MJO has been confined to a smaller sector of the equator, but has a stronger maximum ascent. The maximum in subsidence now occurs immediately ahead of the region of deep convection. The intraseasonal first baroclinic vertical velocities for the Q100 case (Fig. 9c) greatly resemble those of the Q50 case.

The residual WPC1 structures (the full intraseasonal vertical velocity minus the contribution of the first baroclinic mode) for each experiment are shown as the shading in Fig. 9. For all three experiments, the residual structure is dominated by a region of shallow convection ahead of the reference longitude and stratiform convection trailing. In the Q25 experiment, this region of shallow convection extends more than 180° ahead of the reference longitude. For the Q50 experiment, the shallow convection has been confined to a smaller extent ahead of the MJO center, but has increased in magnitude. Additionally, the region of upper-tropospheric subsidence above the shallow convection has increased in strength. More complex structures of vertical velocity start to become more prominent away from the reference longitude. The Q100 experiment exhibits a similar structure, but the shallow convection has weakened significantly and does not penetrate as far into the lower troposphere, nor as far ahead of the reference longitude.

4. Sensitivity of the MJO to model parameters

a. *Sensitivity to mixed layer depth*

We now perturb a few important model parameters to test the sensitivity of the MJO mode. The first parameter we vary is the depth of the ocean mixed layer by performing experiments in the Q50 configuration with the ML depth set to 0.1, 20, and 100 m. Figure 10 shows the resulting space–time spectra of equatorial precipitation for these runs, with Fig. 10a corresponding to the very shallow 0.1-m case. The shallow case produces no significant variability in the MJO spectral region, but instead supports strong Rossby wave variability, as well as other higher-frequency westward-propagating disturbances.

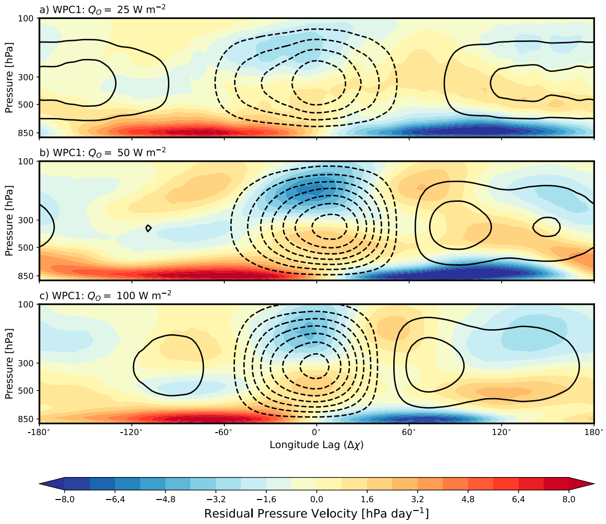

FIG. 9. Equatorial plane of WPC1 for the first baroclinic mode of the intraseasonally filtered vertical velocity (black contours) and the residual structure (shading) for the (a) Q25, (b) Q50, and (c) Q100 experiments. The contour interval is 4 hPa day^{-1}, with negative values dashed and the zero contour omitted. Note the scale of the color bar for the shaded anomalies.

The spectra for the runs with mixed layer depths of 20 and 100 m are shown in Figs. 10b and 10c, respectively. The two deeper mixed layer cases look very similar in all spectral regions. In particular, there is more significant high-frequency Kelvin wave activity when deeper mixed layers are used, and weakened MJO-like variability, although there is still a significant signal along the 6 m s^{-1} phase speed line at intraseasonal time scales. In a zonally symmetric state, deeper mixed layers are less favorable to producing MJO-like variability; whereas the control run with a mixed layer depth of 1 m still produced some weak signal in the MJO spectral region (Fig. 5a), a mixed layer depth of 20 m produces no significant MJO-like variability and instead supports planetary-scale Kelvin waves (not shown). These sensitivity experiments show that our model reproduces the nonmonotonic dependence of intraseasonal variability on ML depth observed in Maloney and Sobel (2004). We see a similar maximum in variability, although at a shallower ML depth than Maloney and Sobel (2004) due to the lack of clouds and corresponding weaker modulation of surface shortwave fluxes on intraseasonal time scales in our model.

Altering the ML depth of the model also has an impact on the spatial distribution of precipitation within the simulated MJO. With a deeper slab the position of the off-equatorial precipitation anomalies associated with the Rossby gyre component of the MJO is shifted significantly eastward relative to both the observed MJO and our simulation with a mixed layer depth of 1 m (Fig. 7b). This shift lends a horizontal structure to the MJO that is mirrored relative to its usual distribution; the usual swallow-tail shape of the MJO points in the opposite direction (not shown). This suggests that while the Kelvin-like component of the MJO mode is rather insensitive to a weakening of ocean coupling, the Rossby-like component is more strongly controlled by circulations induced by SST gradients. The low-level convergence leading the center of the MJO seen in Fig. 9 still exists with a deeper ML, albeit with a weaker magnitude (not shown).

b. *Sensitivity to convection scheme parameters*

We next vary the two parameters that control the behavior of the model's convection scheme. We use two additional runs of the model in the Q50 configuration with the $\mathrm{RH_{SBM}}$ parameter decreased to 60% and increased to 80% from its control value of 70%. Space–time spectra of equatorial precipitation for these runs are shown in Fig. 11, with Fig. 11b corresponding to the unperturbed Q50 experiment. When $\mathrm{RH_{SBM}}$ is made smaller (Fig. 11a), the main impact is seen at intraseasonal time scales, both as an increase in the signal strength from equatorial Rossby waves and as a decrease in the signal strength of the MJO. Conversely, upon increasing $\mathrm{RH_{SBM}}$ to 80%, a reduction in Rossby wave signal and increase in MJO signal is observed. Alongside these changes at intraseasonal time scales, increasing $\mathrm{RH_{SBM}}$ also enhances the variability of higher-frequency Kelvin waves at times scales between 2 and 10 days. Frierson (2007a) observed a similar enhancement of convectively coupled equatorial Kelvin wave activity upon increasing $\mathrm{RH_{SBM}}$ over a similar range, before seeing a reduction in spectral power when using values close to saturation ($\mathrm{RH_{SBM}} = 0.95$), but did not see any changes at intraseasonal time scales.

We also run one further experiment with the moist convective adjustment time τ_{SBM} increased to 16 h in the Q50 configuration. This has the effect of weakening the strength of the intraseasonal variability, although the MJO still remains by far the strongest mode of tropical variability. The spurious high-frequency Kelvin wave signal that was present in the unperturbed Q50 experiment is now completely eliminated, consistent with the sensitivity experiments of Frierson (2007a), in which increasing τ_{SBM} to a value of 8 h removed virtually all Kelvin wave variability.

Figure 12 shows a Hovmöller plot of equatorial precipitation for the run with the larger τ_{SBM}. While there are still eastward-propagating disturbances on the intraseasonal time scale, the nature of these disturbances has changed. Whereas the time series in Fig. 4 show their respective MJO events as coherent bands of precipitation propagating eastward across the warm pool, in Fig. 12 the events have more distinct pockets of precipitation that arise progressively eastward with time, while individual pockets move westward. This kind of convective organization is found in the observed MJO as well (Nakazawa 1988; Madden and Julian 1994). Frierson (2007b) found that running the gray-radiation equivalent of this model with $\tau_{\mathrm{SBM}} = 16$ h made tropical precipitation organize into much smaller pockets of intense precipitation dominated by large-scale condensation, in contrast to the more smeared out features observed when the SBM convection scheme was included. It appears that the while the nature of the clusters of convection within the MJO envelope are sensitive to τ_{SBM}, the presence of the envelope itself is rather insensitive, and its existence depends more on the reference state set by the

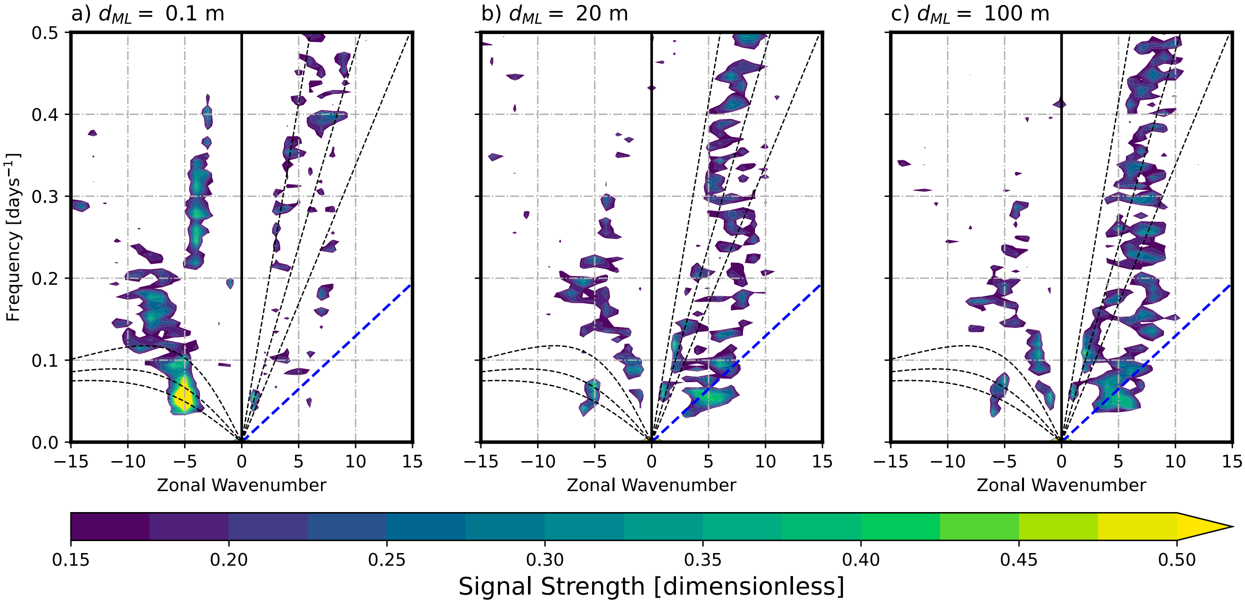

FIG. 10. As in Fig. 5, but for the Q50 configuration with mixed layer depths of (a) 0.1 m, (b) 20 m, and (c) 100 m.

convection scheme through $\mathrm{RH}_{\mathrm{SBM}}$. The analysis of Thayer-Calder and Randall (2009) attributed the weak intraseasonal variability in some GCMs to an overly dry lower troposphere before the onset of convection.

5. Column moist static energy budget

a. *Column moist static energy budget in the GMS plane*

We now examine the column moist static energy (CMSE) budget of the MJO mode produced by our model. We focus here on the Q25 experiment, in which the three-dimensional structure of the simulated MJO mode resembles that of the observed MJO to a reasonable degree. Results for the Q50 and Q100 experiments are qualitatively similar. Analysis of the CMSE budget has been used extensively in past studies of the MJO to identify physical processes that contribute to its destabilization and propagation (Kiranmayi and Maloney 2011; Andersen and Kuang 2012; Arnold et al. 2013; Carlson and Caballero 2016; Yasunaga et al. 2019). The Eulerian budgets for column dry static energy (CDSE) and column

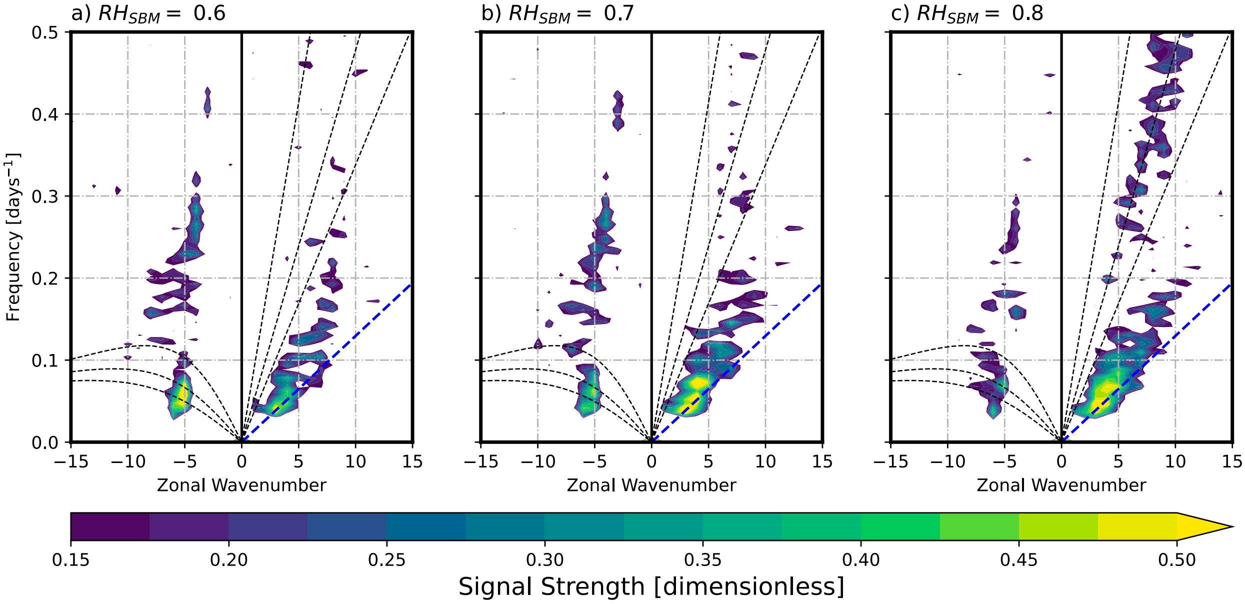

FIG. 11. As in Fig. 5, but for experiments with $\mathrm{RH}_{\mathrm{SBM}}$ set to (a) 60%, (b) 70% (the previously shown Q50 run), and (c) 80%.

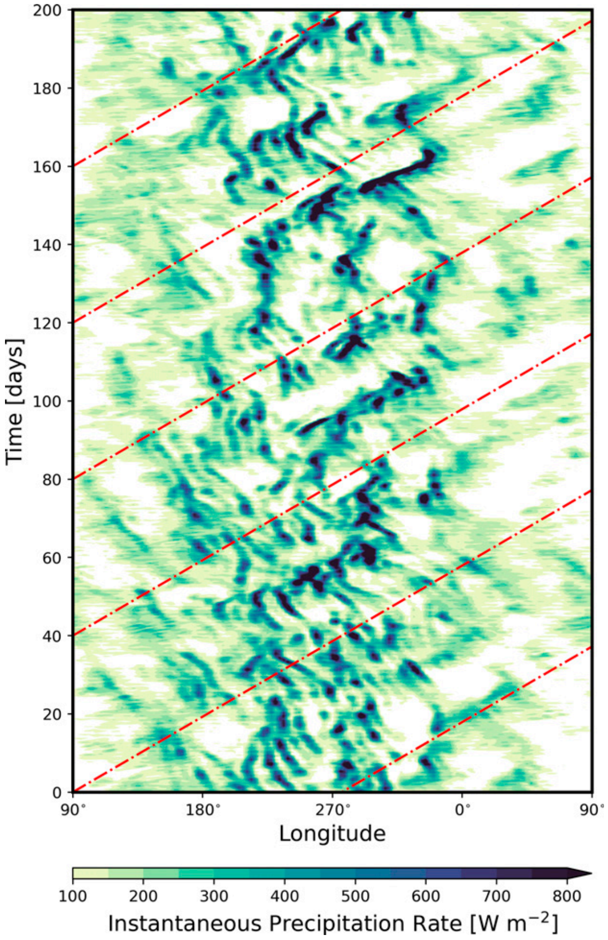

FIG. 12. As in Fig. 4, but for the Q50 experiment with the moist convective adjustment time τ_{SBM} increased to 16 h.

water vapor (CWV) may be combined to form an equation for the CMSE (Yanai et al. 1973; Inoue and Back 2015b, 2017), which takes the form

$$\frac{\partial\langle h\rangle'}{\partial t} = -\nabla\cdot\langle h\mathbf{v}\rangle' + \langle Q_r\rangle' + S', \tag{8}$$

where h is the MSE, $\mathbf{v}$ is the horizontal wind, $\langle Q_r\rangle$ is the radiative heating, and S is the total surface flux of MSE. Angle brackets denote pressure integrals from the surface to 100 hPa where there is assumed to be no vertical motion, and primes denote quantities that have been spectrally filtered to intraseasonal time scales (10–100 days) and eastward wavenumbers 1–10. Following the derivation of Inoue and Back (2015b, 2017), Eq. (8) is then normalized by the anomalous column export of DSE $\nabla\cdot\langle s\mathbf{v}\rangle'$, which acts as a measure of the intensity of convection associated with the MJO. The CMSE budget can then be written in the form

$$\frac{1}{\nabla\cdot\langle s\mathbf{v}\rangle'}\frac{\partial\langle h\rangle'}{\partial t} = -(\Gamma' - \Gamma'_c), \tag{9}$$

where Γ' is the normalized anomalous gross moist stability (GMS) and Γ'_c is termed the normalized anomalous critical GMS. Since in this study we are concerned only with anomalous budgets of CMSE associated with the MJO, for simplicity we will refer to these quantities as the GMS and critical GMS, respectively. These are given by

$$\Gamma' = \frac{\nabla\cdot\langle h\mathbf{v}\rangle'}{\nabla\cdot\langle s\mathbf{v}\rangle'} \quad\text{and}\quad \Gamma'_c = \frac{\langle Q_r\rangle' + S'}{\nabla\cdot\langle s\mathbf{v}\rangle'}. \tag{10}$$

We can further decompose the GMS into its separate contributions from the horizontal and vertical advection of MSE by defining the horizontal and vertical GMS as

$$\Gamma'_h = \frac{\langle\mathbf{v}\cdot\nabla h\rangle'}{\nabla\cdot\langle s\mathbf{v}\rangle'} \quad\text{and}\quad \Gamma'_v = \frac{\langle\omega\partial h/\partial p\rangle'}{\nabla\cdot\langle s\mathbf{v}\rangle'}. \tag{11}$$

In a similar manner, the horizontal GMS can be further decomposed into its contributions from zonal and meridional advection Γ'_x and Γ'_y, and the critical GMS can be decomposed into contributions from radiative heating $\Gamma'_r = \langle Q_r\rangle'/\nabla\cdot\langle s\mathbf{v}\rangle'$ and surface fluxes $\Gamma'_s = S'/\nabla\cdot\langle s\mathbf{v}\rangle'$. The difference between the GMS and critical GMS, Γ'–Γ'_c, is termed the drying efficiency. Inoue and Back (2017) showed that the GMS is a highly time-dependent quantity, but within that time dependence is a coherent cycle in the so-called GMS plane of column export of DSE and MSE. A characteristic value of the GMS over the entirety of this cycle can then be determined via linear regression of the points in this plane, and the cycling behavior may be summarized by considering the GMS as a complex-valued parameter.

We employ the concept of the GMS plane to look at the time-dependent behavior of the CMSE budget. The MJO-filtered time series of $\partial\langle h\rangle'/\partial t$, $\nabla\cdot\langle h\mathbf{v}\rangle'$, and $\langle Q_r\rangle' + S'$ are plotted against the column export of DSE $\nabla\cdot\langle s\mathbf{v}\rangle'$ for all equatorial points from the center of the warm pool (5°S–5°, 210°–330°E). Following Inoue and Back (2017), the characteristic GMS value is calculated as

$$\mathrm{Re}(\Gamma) = \frac{\{(\nabla\cdot\langle h\mathbf{v}\rangle')(\nabla\cdot\langle s\mathbf{v}\rangle')\}}{\{(\nabla\cdot\langle s\mathbf{v}\rangle')(\nabla\cdot\langle s\mathbf{v}\rangle')\}}, \tag{12}$$

where the curly braces indicate an average across all times and spatial points. The imaginary part of the GMS, which measures the degree to which the GMS fluctuates around its characteristic value is given by

$$\mathrm{Im}(\Gamma) = -\lambda_c\frac{\{(\nabla\cdot\langle h\mathbf{v}\rangle')(\partial\nabla\cdot\langle s\mathbf{v}\rangle'/\partial t)\}}{\{(\partial\nabla\cdot\langle s\mathbf{v}\rangle'/\partial t)(\partial\nabla\cdot\langle s\mathbf{v}\rangle'/\partial t)\}}, \tag{13}$$

where λ_c is a characteristic frequency for the MJO. For the MJO mode simulated by our model, we take this frequency to be 2π (30 days)$^{-1}$. Definitions for the characteristic and fluctuating values of the critical GMS and drying efficiency are defined in a similar manner.

Figure 13 shows the resulting orbits in the GMS plane for the MJO-filtered time series of the CMSE budget terms using data from the center of the warm pool (5°S–5°N, 210°–330°E) in the Q25 experiment. The scatterplot of column export of MSE versus column export of DSE in shown in Fig. 13a. Linear regression through the origin gives a positive characteristic GMS (note that in the figure the column export of

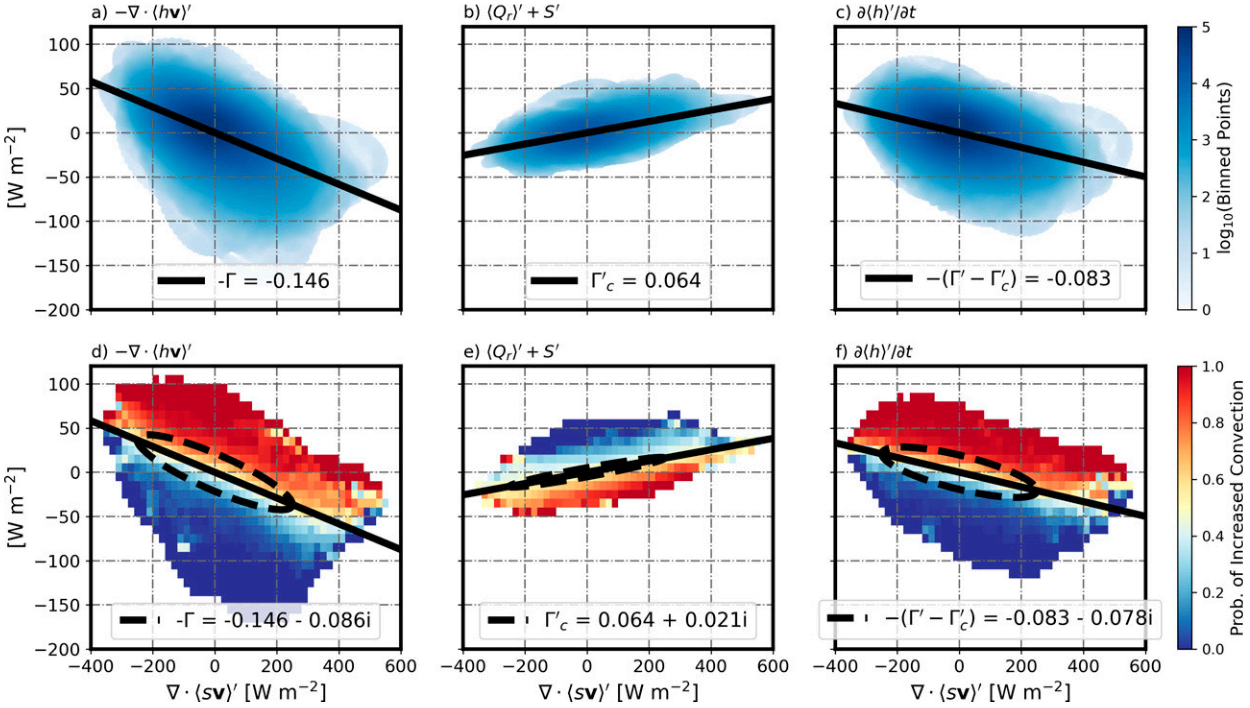

FIG. 13. Convective life cycle of the CMSE budget using data from the center of the warm pool (5°S–5°N, 210°–330°E) in the Q25 experiment. (a) Scatterplot of $-\nabla\cdot\langle h\mathbf{v}\rangle'$ vs $\nabla\cdot\langle s\mathbf{v}\rangle'$; darker colors indicate a denser collection of scatter points, and the solid black line shows a regression through the origin. (b) As in (a), but for the diabatic source $\langle Q_r\rangle' + S'$ vs $\nabla\cdot\langle s\mathbf{v}\rangle'$. (c) As in (a), but for the CMSE time tendency $\partial\langle h\rangle'/\partial t$ vs $\nabla\cdot\langle s\mathbf{v}\rangle'$. (d) Scatterplot of $-\nabla\cdot\langle h\mathbf{v}\rangle'$ vs $\nabla\cdot\langle s\mathbf{v}\rangle'$, gridded and colored by the fraction of points in each grid box in which the convection intensifies; the dashed black line shows the linearly regressed orbit in the GMS phase plane for convection with an amplitude of 100 W m^{-2}. (e) As in (d), but for $\langle Q_r\rangle' + S'$. (f) As in (d), but for $\partial\langle h\rangle'/\partial t$.

MSE has been multiplied by -1), so that at the time of maximum convection the combination of horizontal and vertical advection is removing MSE from the column. Figure 13d shows the same scatterplot, but with colors indicating the fraction of points in which the strength of convection is increasing (i.e., $\partial\nabla\cdot\langle s\mathbf{v}\rangle'/\partial t > 0$). The times at which convection is increasing are associated with negative GMS, so that the combination of horizontal and vertical advection is acting to import MSE into the column. At times when convection is weakening, the GMS is higher than its characteristic value, and advection acts to damp CMSE anomalies. When the column export of MSE is decomposed into its contributions from horizontal and vertical advection, it is found that the cycling behavior of the GMS is driven by horizontal advection, while the value of the characteristic GMS is determined primarily by vertical advection (see Table 1). Inoue and Back (2015a) found similar contributions from vertical and horizontal advection at intraseasonal time scales.

Figures 13b and 13e show the combined contribution to the CMSE tendency from radiative heating and surface MSE fluxes. These two separate terms contribute roughly equal parts to the characteristic value of Γ_c'. The radiative heating component is strongly coupled to the strength of convection, and does not fluctuate around its characteristic value (not shown). The strength of the radiative heating is also weak compared to its observed effect on Earth: anomalous radiative heating associated with the MJO is observed to be roughly linearly related to anomalous precipitation as

$$\langle Q_r\rangle' = rL_vP', \tag{14}$$

where r is a cloud-radiative feedback parameter (Kim et al. 2015; Adames and Kim 2016), which generally takes on a value of $r \approx 0.17$, though Adames and Kim (2016) suggested that this parameter may have some scale dependence, so that planetary-scale motions feel a stronger feedback than those at smaller scales. Parameters of this kind have seen extensive use in theoretical models of the MJO (Fuchs and Raymond 2002; Sobel and Maloney 2012; Adames and Kim 2016; Fuchs and Raymond 2017). Under the WTG approximation, in which the time tendency of CDSE is ignored (Inoue and Back 2015b), and neglecting surface sensible heat fluxes, the CDSE budget may be written as

$$0 = -\nabla\cdot\langle s\mathbf{v}\rangle' + \langle Q_r\rangle' + L_vP'. \tag{15}$$

The radiative heating GMS can then be related to the cloud-radiative feedback parameter as

$$r = \frac{\Gamma_r'}{1 - \Gamma_r'}. \tag{16}$$

In our model, where $\Gamma_r' \approx 0.03$, we will have $\Gamma_r' \approx r$. Thus the value of r in our model is much weaker than observed for

TABLE 1. Summary of GMS parameters calculated for the each individual term of the MJO-filtered CMSE budget for the control, Q25, Q50, and Q100 experiments along with the runs with varied ML depth. Real parts of the parameters are the contribution to maintenance, and imaginary parts are the contribution to propagation (Inoue and Back 2017). Note that the advective and diabatic GMS parameters enter into the normalized CMSE equation with different signs.

Term	Numerator	Control	Q25	Q50	Q100	ML0.1	ML20	ML100
Γ'_x	$\langle u\partial h/\partial x\rangle'$	$-0.04 - 0.01i$	$-0.02 + 0.01i$	$0.01 + 0.02i$	$0.03 + 0.03i$	$-0.03 + 0.00i$	$0.03 + 0.02i$	$0.02 + 0.01i$
Γ'_y	$\langle v\partial h/\partial y\rangle'$	$-0.04 + 0.07i$	$-0.05 + 0.06i$	$-0.05 + 0.05i$	$-0.08 + 0.04i$	$-0.09 + 0.07i$	$-0.03 + 0.05i$	$-0.04 + 0.05i$
Γ'_v	$\langle \omega\partial h/\partial p\rangle'$	$0.22 + 0.03i$	$0.22 + 0.02i$	$0.21 + 0.01i$	$0.20 + 0.01i$	$0.21 + 0.02i$	$0.21 + 0.01i$	$0.21 + 0.01i$
Γ'_r	$\langle Q_r\rangle'$	$0.03 + 0.01i$	$0.03 + 0.00i$	$0.03 + 0.00i$	$0.03 + 0.00i$	$0.03 + 0.00i$	$0.02 + 0.00i$	$0.02 + 0.00i$
Γ'_s	S'	$0.02 + 0.02i$	$0.04 + 0.02i$	$0.05 + 0.02i$	$0.04 + 0.02i$	$0.00 + 0.01i$	$0.12 + 0.03i$	$0.09 + 0.03i$
Γ'–Γ'_c	$-\partial\langle h\rangle'/\partial t$	$0.08 + 0.08i$	$0.08 + 0.08i$	$0.10 + 0.08i$	$0.10 + 0.07i$	$0.08 + 0.10i$	$0.07 + 0.06i$	$0.07 + 0.06i$

Earth. This is not surprising; since our model has no clouds it relies only on radiation–water vapor interactions to produce this effect. However, cloud-radiative effects have been shown to be important for moisture mode instability by reducing the effective GMS (Sobel and Maloney 2012; Adames and Kim 2016; Adames et al. 2019) that the MJO feels. It is interesting that our model is able to produce an MJO-like intraseasonal mode with this effect severely diminished.

The surface MSE flux provides resistance to the propagation of the MJO by orbiting around its characteristic value in an opposite sense to GMS, and maintains the MSE anomalies at the time of strongest convection. Surface fluxes of sensible heat are small in the tropics (Inoue and Back 2017), so this term is dominated by the contribution from surface latent heat flux. This is consistent with the results of Adames (2017), who found that MJO-related surface evaporation anomalies played an analogous role in opposing the propagation of MJO precipitation, which should be approximately collocated with CMSE anomalies close to the equator.

Figures 13c and 13f show the convective life cycle of the time tendency of CMSE. Like the GMS, the drying efficiency exhibits a wide orbit, which allows disturbances to continue to grow into the convectively active phase despite the characteristic value of drying efficiency being positive. The cycles of the individual budget terms should sum to this cycle. In reality, there will be a residual contribution due in part to the fact that the radiative heating rate, which is a model diagnostic, is integrated to the top of the atmosphere, while the advection terms of our budget are integrated to the assumed rigid lid at 100 hPa. The residuals are however small compared to the magnitude of the drying efficiency, suggesting that the budget is still approximately closed.

Table 1 shows the contributions to the drying efficiency from each term in the CMSE budget for the four core experiments and ML depth experiments. As expected, the strength of the surface flux feedback is sensitive to the ML depth and is virtually eliminated in the very shallow case, but the horizontal advection terms adjust so that the drying efficiency is still similar to the core experiments. Budgets for the runs with different $\mathrm{RH}_{\mathrm{SBM}}$ were very similar to the Q50 experiment about which they are perturbed. The extended moist convective adjustment time run (where $\tau_{\mathrm{SBM}} = 16$ h) did not reproduce the same strong coupling between vertical MSE advection and convection seen in all other experiments. Given the more chaotic organization of convection in this experiment, it seems that the simple spectral filtering used here is unable to reliably diagnose the CMSE budget for this specific run.

Inoue and Back (2015b) showed that when a region is convectively active ($\nabla \cdot \langle s\mathbf{v}\rangle' > 0$), the sign of the drying efficiency identifies two different phases of the MJO: A negative drying efficiency corresponds to the amplification of convection while a positive drying efficiency corresponds to the decay of convection. The CMSE budget can then be viewed as a function of the drying efficiency itself, to see how the behavior of the budget changes as the convective life cycle evolves. Figure 14 shows this evolution of the GMS and critical GMS as functions of the drying efficiency using the GMS plane orbits found in Fig. 13. The trajectories of the GMS parameters are linear functions of the drying efficiency. Binning the MJO-filtered time series of Γ' and Γ'_c by their drying efficiency produces similar linear trajectories (not shown). During the amplifying phase, the GMS (the red line) destabilizes the MJO mode, then switches sign and becomes a stabilizing influence during the decaying phase. The critical GMS (the blue line), which is dominated by the contribution from surface fluxes, provides opposition to the propagation of the MJO, indicated by the negative slope as a function of the drying efficiency. Thus the critical GMS acts opposite to the GMS, stabilizing the MJO during its amplifying phase and destabilizing it during the decaying phase of convection. A small residual (the gray line) exists since the drying efficiency is calculated from the time tendency of CMSE, while the GMS and critical GMS are calculated using advective and flux terms, respectively.

b. Connection to linear theories of the MJO

If we consider the MJO in a linear wave framework as an equatorially trapped Fourier mode with wavenumber k and complex frequency λ, then the GMS quantities that were calculated in section 5a become parameters of the linear model. In such a framework, the vertical velocity field may be assumed to be truncated to a single vertical mode that corresponds to deep convection throughout the depth of the troposphere (Fuchs and Raymond 2017; Adames et al. 2019). The anomalous vertical velocity related to the MJO can then be written as

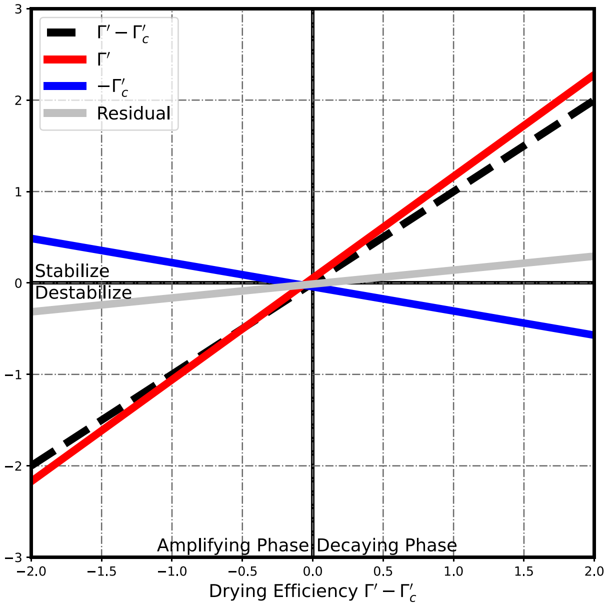

FIG. 14. Normalized CMSE budget of the simulated MJO budget in the Q25 experiment as a function of the drying efficiency. The GMS plane orbits of the GMS Γ' (red line), critical GMS Γ'_c (blue line), and drying efficiency (Γ'–Γ'_c) (black dashed line) from Fig. 13 are plotted as functions of the drying efficiency itself. The residual of the CMSE budget is shown as a gray line.

$$\omega' = \omega_1 D_\omega(y)\Lambda_\omega(p) = \hat{\omega}_1 D_\omega(y)\Lambda_\omega(p)e^{i(kx-\lambda t)}, \tag{17}$$

where $\hat{\omega}_1$ is the amplitude of the vertical velocity, $D_\omega(y)$ its meridional structure, and $\Lambda_\omega(p)$ its vertical structure. The column export of DSE (which was used previously to measure the strength of convection) is tightly coupled to the first baroclinic vertical velocity, so that the gross dry stability M_s can be introduced to satisfy $-\nabla \cdot \langle s\mathbf{v}\rangle' = M_s\omega_1$. A value for M_s is determined in a similar manner to how the GMS parameters of section 5a were calculated, with M_s assumed to be real-valued. The CMSE budget given in Eq. (8) may then be written as

$$-i\lambda\langle h\rangle' = \Gamma^*(\lambda, k)M_s\omega_1, \tag{18}$$

where $\Gamma^*(\lambda, k)$ is some general phase relation that depends on the specific physical parameterizations introduced by a linear model. For example, surface MSE fluxes and zonal MSE advection could be parameterized using the wind-induced surface heat exchange (WISHE) mechanism (Neelin et al. 1987; Emanuel 1987), which introduces a dependence on the zonal scale of the wave and prefers instability at planetary scales (Fuchs and Raymond 2005, 2017). Similarly, radiative heating could be related to the precipitation rate through the cloud-radiative feedback parameter (Adames and Kim 2016; Adames et al. 2019), which can then be related back to the vertical velocity field through the CDSE equation. Here the focus will be on the simplest treatment possible for the CMSE equation, where Eq. (18) can be written in terms of the drying efficiency as

$$-i\lambda\langle h\rangle' = (\Gamma - \Gamma_c)M_s\omega_1, \tag{19}$$

where the drying efficiency $\Gamma - \Gamma_c$ is a complex parameter that does not depend on λ or k. This formulation implicitly includes contributions from higher-order vertical modes; the contribution to the drying efficiency from vertical advection is calculated using the full vertical velocity field, rather than only the first baroclinic mode, so that the recharging of CMSE by shallow convection ahead of the MJO deep convection is still included. For simplicity, we will consider the case of no meridional flow ($v = 0$). Such frameworks have been used in the past to gain insight into the MJO and other equatorially trapped waves (Fuchs and Raymond 2017; Adames et al. 2019; Ahmed 2021). With no meridional flow, the meridional momentum equation reduces to a Sverdrup balance which gives the meridional structure that is common to all fields in the model. With this assumption only eastward-propagating modes may exist, as westward modes ($k < 0$) will not decay away from the equator. The appendix shows that the CDSE may be approximated as $\langle s\rangle' \approx iM_s\lambda\omega_1/(c^2k^2)$, where c is the phase speed of dry gravity waves and is given by $c = [R_dM_s/(C_p\langle\Lambda_T\rangle)]^{1/2}$, where R_d is the specific gas constant for air, C_p the specific heat capacity, and $\langle\Lambda_T\rangle$ the pressure integral of the vertical structure of the temperature field. This gives a dry gravity wave speed of $c \approx 51$ m s^{-1}, close to observed values for Earth (Kiladis et al. 2009). The governing equations for the system are then given by

$$\frac{M_s}{c^2}\frac{\lambda^2}{k^2}\omega_1 = M_s\omega_1 + L_vP' \quad \text{and} \tag{20a}$$

$$-i\lambda\langle h\rangle' = (\Gamma - \Gamma_c)M_s\omega_1, \tag{20b}$$

where the contributions to the CDSE tendency from radiative heating and surface sensible heat fluxes have been neglected as being small relative to the precipitation term.

To close the system of equations, a parameterization of the precipitation term is required. This is done via a Betts–Miller-type closure of the form

$$L_vP' = \frac{L_v}{\tau_c}\langle q\rangle' = \frac{1}{\tau_c}\left(\langle h\rangle' - i\frac{M_s}{c^2}\frac{\lambda}{k^2}\omega_1\right), \tag{21}$$

where τ_c is a moist convective relaxation time scale. Such closures have been used extensively in previous linear theories of the MJO and other equatorial disturbances (Sobel and Maloney 2012; Adames and Kim 2016; Fuchs and Raymond 2017; Adames et al. 2019). Figure 15a shows a representation of τ_c in the phase plane of MJO-related precipitation and CWV. Note that τ_c exhibits a small orbit around its characteristic value, but is still tightly coupled to the precipitation. Thayer-Calder and Randall (2009) also found cyclical paths in the MJO precipitation-CWV phase plane using both model and observational data. We find that $\tau_c \approx 9.5$–$1.8i$ h, shorter than the values used in Adames and Kim (2016) and Adames et al. (2019), but still distinct from the model's convective adjustment time, $\tau_{\mathrm{SBM}} = 2$ h.

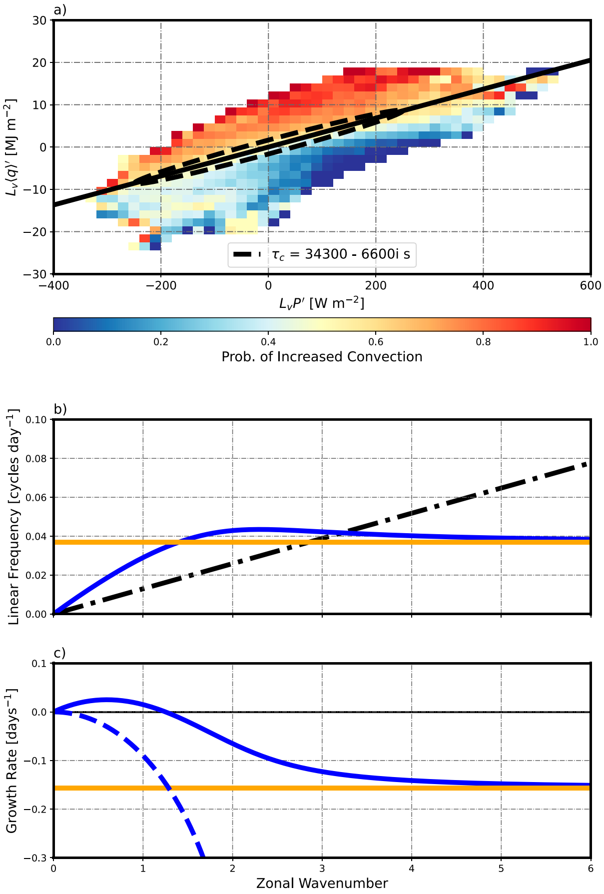

FIG. 15. (a) Representation of τ_c in the phase plane of MJO precipitation and CWV. (b) Linear frequency Re(λ)/(2π) for the undamped mode of the full dispersion relation (blue line) and the simplified WTG solution (orange line). The black dash-dotted line shows the 6 m s^{-1} phase speed line. (c) Growth rate for the undamped mode of the full dispersion relation (blue line) and the WTG solution (orange line). The dashed blue line shows the solution of the full dispersion relation when the imaginary part of the drying efficiency is neglected.

With this parameterization in hand, the anomalous CMSE $\langle h\rangle'$ may be eliminated between Eqs. (20a) and (20b) to get the following dispersion relation:

$$\tau_c\lambda^3 + i\lambda^2 - c^2k^2\tau_c\lambda - ic^2k^2(\Gamma - \Gamma_c) = 0. \qquad (22)$$

As in Fuchs and Raymond (2017) and Adames et al. (2019), this relation yields two damped modes and a single undamped mode at planetary scales. The solid blue lines in Figs. 15b and 15c show the frequency and growth rate of this unstable mode, respectively. As in Fuchs and Raymond (2017), this $v = 0$ mode has a faster phase speed than the observed MJO (shown by the black dash-dotted line in Fig. 15b). The mode also exhibits a westward group velocity for $k > 2$. The growth rate of the mode remains positive for a range of k that extends just slightly past $k = 1$, and has a weaker magnitude than the solutions of Fuchs and Raymond (2017) and Adames et al. (2019).

This dispersion relation may be simplified by neglecting the second- and third-order terms in λ. Physically, this is equivalent to invoking the WTG approximation: the time tendency of the CDSE is assumed to be small, and the time tendency of the CMSE is then assumed to be dominated by its contribution from the moisture tendency. Equations (20a) and (20b) may then be written as

$$0 = M_s\omega_1 + L_vP' \quad \text{and} \qquad (23a)$$

$$-i\lambda\left(\langle h\rangle' - i\frac{M_s}{c^2}\frac{\lambda^2}{k^2}\omega_1\right) = (\Gamma - \Gamma_c)M_s\omega_1. \qquad (23b)$$

Solving this system for λ then yields the simplified dispersion relation

$$\lambda = -\frac{i}{\tau_c}(\Gamma - \Gamma_c). \qquad (24)$$

In this WTG setting, the real part of the drying efficiency determines whether the mode will be unstable, and the imaginary part determines the speed at which the wave propagates. The solid orange lines in Figs. 15b and 15c show the linear frequency and growth rate of this mode. Both the frequency and the growth rate of the mode are insensitive to the zonal scale of the wave. Due to the weak radiative heating associated with the MJO in our model, the mode is damped and cannot be destabilized in a WTG setting. This is in contrast to the $v = 0$ WTG mode discussed in Adames et al. (2019), where strong cloud–radiation interactions adequately lowered the effective GMS to make the mode unstable at planetary scales. Fuchs and Raymond (2017) also found that their WISHE moisture mode was damped in a WTG setting in the absence of cloud-radiative feedbacks.

The dashed blue line in Fig. 15c shows the growth rate of the mode when the imaginary parts of $\Gamma - \Gamma_c$ and τ_c are neglected. Making this alteration eliminates the instability at planetary scales. This suggests that the convective life cycle of the column export of MSE, which is encapsulated by allowing the GMS parameters and hence the drying efficiency to be complex-valued, is essential to the existence of an instability at planetary scales in the absence of strong WISHE or cloud-radiative feedbacks.

6. Discussion and summary

In this study we have shown that MJO-like variability may be induced in an idealized moist GCM without any parameterization of clouds by introducing zonal asymmetry through an equatorially trapped wavenumber-1 ocean heat flux. The simulated MJO was able to reproduce many of the characteristics of the observed MJO: slow (6 m s^{-1}) propagation eastward across the warm pool sector, swallow-tail spatial structure of precipitation, and westward tilt with height were all reproduced by the model. The strength of this MJO mode was strongest when the surface temperature contrast between the warm pool and cold pool was around 5 K (the Q50 experiment). Further increasing the asymmetry produced a peculiar bistable regime, where high-frequency Kelvin waves and the MJO mode dominated tropical variability at different times. The application of this asymmetric forcing also had profound effects on the mean state of the simulations; a transition to superrotation in the tropical upper troposphere and a weakening of the Hadley cell were observed as the contrast between the cold pool and warm pool was increased. This was accompanied by a moistening of the subtropics of the cold hemisphere, so that thermodynamic fields take on a KR pattern. However, the meridional MSE transport was insensitive to the imposition of this zonal asymmetry, as the prescribed wavenumber-1 pattern adds no additional energy to the model in the zonal mean.

The MJO mode generated in our model was sensitive to the ML depth of the underlying slab ocean. Due to the absence of clouds in the model (and hence weak modulation of surface downward shortwave flux relative to Earth), a shallow ML depth (1 m) was required to produce intraseasonal SST fluctuations commensurate with the observed MJO. Deeper slabs lead to weaker intraseasonal variability, consistent with the study of Maloney and Sobel (2004). An experiment with a very shallow depth of 0.1 m eliminated the MJO-like variability, reproducing the nonmonotonic ML dependency reported in Maloney and Sobel (2004) and Sobel and Gildor (2003), albeit in a different range of ML depths. The behavior of the MJO mode was also found to be sensitive to the configuration of the model's convection scheme. Upon increasing (decreasing) the relative humidity of the reference moisture profile the MJO mode became stronger (weaker), consistent with a disparate set of moist convection parameterizations (Wang and Schlesinger 1999). Interestingly, the MJO-like variability is retained when the moist convective adjustment time of the convection scheme was increased to 16 h; this alteration drastically changed the way equatorial precipitation organized, yet precipitation anomalies were still seen to propagate slowly across the warm pool sector. It is one of the strengths of our study that there are only two parameters to adjust in the SBM convection scheme; studies using more comprehensive GCMs (e.g., Hannah and Maloney 2014; Klingaman and Woolnough 2014a,b) have shown a strong dependence on the parameters of more complicated convection schemes.

It is the generation of an MJO-like disturbance without any contribution from cloud-radiative feedbacks that is perhaps the most interesting result of this study. Previous studies using a variety of more complex GCMs (Andersen and Kuang 2012; Arnold et al. 2013; Carlson and Caballero 2016; Khairoutdinov and Emanuel 2018) have shown that radiative feedbacks play a vital role in destabilizing the MJO, although Arnold and Randall (2015) showed that models with superparameterized convection may still produce MJO-like variability with this feedback suppressed. An analysis of the CMSE budget of the simulated MJO mode revealed that horizontal advection of MSE plays a dominant role in setting the "drying efficiency" of the atmosphere throughout the convective life cycle of the MJO. Prior to the arrival of the MJO, horizontal advection acts to charge the column with MSE before transitioning to removing MSE from the column when convection is at a maximum. Due to the lack of any clouds in the model, the contribution to destabilization from radiative heating was weak. Therefore at the time of maximum convection the MJO column process, the sum of the vertical advection and diabatic terms (Chikira 2014; Wolding and Maloney 2015), is negative and stabilizes the anomalies of CMSE. In this sense, the MJO produced by our model fits better into the recharge–discharge paradigm (Bladé and Hartmann 1993; Hu and Randall 1994) than the concept of moisture mode instability, wherein strong radiative feedbacks overcome the stabilizing contribution of vertical MSE advection to produce instability at the time of maximum convection. Recent reanalysis and comprehensive modeling studies have argued that the moisture mode instability is the more relevant picture for more realistic representations of the MJO (Chikira 2014; Wolding and Maloney 2015), so it is interesting that our model is able to reproduce many of the most distinct features of the MJO without this instability being active. Furthermore, it is compelling that, similar to Bladé and Hartmann (1993), zonal asymmetry is required for our recharge–discharge MJO to become a prominent mode of variability.

A linear stability analysis in the simplified case where $v = 0$ using parameters derived from our model suggested that instability may be produced at planetary scales without appealing to either WISHE or cloud-radiative feedbacks to act as a destabilizing influence. In particular, modeling the convective life cycle of the MJO mode by allowing the drying efficiency and moist convective adjustment time to be complex-valued parameters was found to be essential to producing a planetary-scale instability. Enforcing WTG balance led to the mode being damped equally at all length scales, as the convection–radiation feedbacks were too weak to sufficiently reduce the effective GMS as is required in other moisture mode theories (Adames et al. 2019), reinforcing the idea that the traditional moisture mode instability, which depends on the real part of the drying efficiency (Inoue and Back 2017), is not active in our model. While the linear theory presented in this study provides a simple picture of intraseasonal variability, it is also a gross simplification of the nonlinear dynamics of our numerical model. While it is a useful tool to understand the role of moisture mode instability in our model, it should not be expected to explain the more subtle features of the MJO mode.

The analysis performed in this study has been from a column-integrated viewpoint of the MJO. While this provides a simple framework in which to identify instability mechanisms, it can also obscure the role of boundary layer processes. While we have primarily interpreted the simulated MJO mode through the lens of moisture mode instability and the recharge–discharge hypothesis, the theory of three-way ("trio") interaction (Wang et al. 2016; Wang and Chen 2017) puts forth frictional moisture convergence in the boundary layer as an additional essential component to the MJO. Future work should look at understanding the role of the boundary layer in forcing the observed life cycle of MJO convection in this idealized model. The role of the extratropics in forcing the intraseasonal variability in our model is another outstanding uncertainty in these simulations. Extratropical initiation of MJO events was identified as being important in the study of Bladé and Hartmann (1993), and more recent work has emphasized the importance of this mechanism (Ray et al. 2009; Ray and Zhang 2010). The simplified GCM used in this study provides a valuable opportunity to explore the global interactions of MJO-like variability.

Acknowledgments. The authors acknowledge GFDL resources made available for this research. The authors thank Spencer Clark for assistance in configuring and running the numerical model used in this study. Comments from Isaac Held and Ángel Adames-Corraliza greatly improved the quality of the manuscript. Finally, the authors thank three anonymous reviewers for their helpful comments.

Data availability statement. The numerical experiments performed in this study were carried out using the National Oceanic and Atmospheric Administration (NOAA) Geophysical Fluid Dynamics Laboratory's (GFDL) Flexible Modeling System (FMS). FMS can be accessed at https://www.gfdl.noaa.gov/fms/.

APPENDIX

Phase Relation between CDSE and First Baroclinic Pressure Velocity

The linearized, $v = 0$ momentum, continuity, and hydrostatic equations truncated to a first baroclinic mode on the equatorial β plane are given by (e.g., Fuchs and Raymond 2017; Adames et al. 2019)

$$\frac{\partial u'}{\partial t} = -\frac{\partial \phi'}{\partial x}, \tag{A1a}$$

$$\beta y u' = -\frac{\partial \phi'}{\partial y}, \tag{A1b}$$

$$\frac{\partial u'}{\partial x} = -\frac{\partial \omega'}{\partial p}, \quad \text{and} \tag{A1c}$$

$$\frac{\partial \phi'}{\partial \ln p} = -R_d T', \tag{A1d}$$

where u' is the zonal velocity anomaly, ϕ' is the geopotential anomaly, T' is the temperature anomaly, and β is the meridional gradient of the planetary vorticity. We first note that eliminating u' between Eqs. (A1a) and (A1b) provides the meridional structure $D(y)$ that is common to all the fields, which must satisfy

$$\frac{dD(y)}{dy} = -\frac{\beta k}{\lambda} y D(y). \tag{A2}$$

This equation can be solved to yield a meridional structure given by

$$D(y) = \exp\left(-\frac{\beta k}{2\lambda} y^2\right), \tag{A3}$$

which limits our solutions to only eastward propagating modes, as westward modes ($k < 0$) will not decay away from the equator. Equation (A1) also stipulates certain relations between the vertical structures of the various fields. The conditions provided by the zonal momentum, continuity, and hydrostatic equations are respectively given by

$$\Lambda_u(p) = \Lambda_\phi(p), \tag{A4a}$$

$$\Lambda_u(p) = -\frac{d\Lambda_\omega(p)}{dp}, \quad \text{and} \tag{A4b}$$

$$\frac{d\Lambda_\phi(p)}{d\ln p} = \Lambda_T(p). \tag{A4c}$$

Removing the common vertical and meridional dependence, Eqs. (A1a), (A1c), and (A1d) may be expressed as

$$\lambda u_1 = k\phi_1, \tag{A5a}$$

$$iku_1 = \omega_1, \quad \text{and} \tag{A5b}$$

$$\phi_1 = -R_d T_1. \tag{A5c}$$

The anomalous DSE is given by $s' = C_p T' + \phi'$, so that the vertically integrated anomalous DSE may be written as

$$\langle s\rangle' = R_d T_1 (C_p \langle \Lambda_T\rangle / R_d - \langle \Lambda_\phi \rangle), \tag{A6}$$

where Eq. (A5c) has been used to relate the geopotential anomaly to the temperature anomaly. The term in the parentheses is dominated by its first term, related to the vertical integral of temperature, so the contribution from $\langle \Lambda_\phi \rangle$ is neglected. Equation (A5) may then be used to relate the vertically integrated DSE anomaly to the pressure velocity as

$$\langle s\rangle' = i\frac{C_p}{R_d}\frac{\lambda}{k^2}\langle \Lambda_T\rangle \omega_1. \tag{A7}$$

The square of the dry gravity wave speed can then be defined as $c^2 = R_d M_s/(C_p\langle \Lambda_T\rangle)$ so that the anomalous CDSE may be written as

$$\langle s\rangle' = i\frac{M_s}{c^2}\frac{\lambda}{k^2}\omega_1. \tag{A8}$$

REFERENCES

Adames, Á. F., 2017: Precipitation budget of the Madden–Julian Oscillation. *J. Atmos. Sci.*, **74**, 1799–1817, https://doi.org/10.1175/JAS-D-16-0242.1.

——, and J. M. Wallace, 2014a: Three-dimensional structure and evolution of the MJO and its relation to the mean flow. *J. Atmos. Sci.*, **71**, 2007–2026, https://doi.org/10.1175/JAS-D-13-0254.1.

——, and ——, 2014b: Three-dimensional structure and evolution of the vertical velocity and divergence fields in the MJO. *J. Atmos. Sci.*, **71**, 4661–4681, https://doi.org/10.1175/JAS-D-14-0091.1.

——, and ——, 2015: Three-dimensional structure and evolution of the moisture field in the MJO. *J. Atmos. Sci.*, **72**, 3733–3754, https://doi.org/10.1175/JAS-D-15-0003.1.

——, and D. Kim, 2016: The MJO as a dispersive, convectively coupled moisture wave: Theory and observations. *J. Atmos. Sci.*, **73**, 913–941, https://doi.org/10.1175/JAS-D-15-0170.1.

——, and E. D. Maloney, 2021: Moisture mode theory's contribution to advances in our understanding of the Madden–Julian oscillation and other tropical disturbances. *Curr. Climate Change Rep.*, **7**, 72–85, https://doi.org/10.1007/s40641-021-00172-4.

——, D. Kim, S. K. Clark, Y. Ming, and K. Inoue, 2019: Scale analysis of moist thermodynamics in a simple model and the relationship between moisture modes and gravity waves. *J. Atmos. Sci.*, **76**, 3863–3881, https://doi.org/10.1175/JAS-D-19-0121.1.

Ahmed, F., 2021: The MJO on the equatorial beta plane: An eastward-propagating Rossby wave induced by meridional moisture advection. *J. Atmos. Sci.*, **78**, 3115–3135, https://doi.org/10.1175/JAS-D-21-0071.1.

Andersen, J. A., and Z. Kuang, 2012: Moist static energy budget of MJO-like disturbances in the atmosphere of a zonally symmetric aquaplanet. *J. Climate*, **25**, 2782–2804, https://doi.org/10.1175/JCLI-D-11-00168.1.

Arnold, N. P., and D. A. Randall, 2015: Global-scale convective aggregation: Implications for the Madden–Julian oscillation. *J. Adv. Model. Earth Syst.*, **7**, 1499–1518, https://doi.org/10.1002/2015MS000498.

——, Z. Kuang, and E. Tziperman, 2013: Enhanced MJO-like variability at high SST. *J. Climate*, **26**, 988–1001, https://doi.org/10.1175/JCLI-D-12-00272.1.

Benedict, J. J., and D. A. Randall, 2007: Observed characteristics of the MJO relative to maximum rainfall. *J. Atmos. Sci.*, **64**, 2332–2354, https://doi.org/10.1175/JAS3968.1.

Betts, A. K., and M. J. Miller, 1986: A new convective adjustment scheme. Part II: Single column tests using GATE wave, BOMEX, ATEX and Arctic air-mass data sets. *Quart. J. Roy. Meteor. Soc.*, **112**, 693–709. https://doi.org/10.1002/qj.49711247308.

Bladé, I., and D. L. Hartmann, 1993: Tropical intraseasonal oscillations in a simple nonlinear model. *J. Atmos. Sci.*, **50**, 2922–2939, https://doi.org/10.1175/1520-0469(1993)050<2922:TIOIAS>2.0.CO;2.

Bretherton, C. S., M. E. Peters, and L. E. Back, 2004: Relationships between water vapor path and precipitation over the tropical oceans. *J. Climate*, **17**, 1517–1528, https://doi.org/10.1175/1520-0442(2004)017<1517:RBWVPA>2.0.CO;2.

Carlson, H., and R. Caballero, 2016: Enhanced MJO and transition to superrotation in warm climates. *J. Adv. Model. Earth Syst.*, **8**, 304–318, https://doi.org/10.1002/2015MS000615.

Chen, G., and B. Wang, 2018: Does the MJO have a westward group velocity? *J. Climate*, **31**, 2435–2443, https://doi.org/10.1175/JCLI-D-17-0446.1.

Chikira, M., 2014: Eastward-propagating intraseasonal oscillation represented by Chikira–Sugiyama cumulus parameterization. Part II: Understanding moisture variation under weak temperature gradient balance. *J. Atmos. Sci.*, **71**, 615–639, https://doi.org/10.1175/JAS-D-13-038.1.

Clark, S. K., Y. Ming, I. M. Held, and P. J. Phillipps, 2018: The role of the water vapor feedback in the ITCZ response to hemispherically asymmetric forcings. *J. Climate*, **31**, 3659–3678, https://doi.org/10.1175/JCLI-D-17-0723.1.

——, ——, and Á. F. Adames, 2020: Monsoon low pressure system–like variability in an idealized moist model. *J. Climate*, **33**, 2051–2074, https://doi.org/10.1175/JCLI-D-19-0289.1.

Emanuel, K. A., 1987: An air–sea interaction model of intraseasonal oscillations in the tropics. *J. Atmos. Sci.*, **44**, 2324–2340, https://doi.org/10.1175/1520-0469(1987)044<2324:AASIMO>2.0.CO;2.

——, 2020: Slow modes of the equatorial waveguide. *J. Atmos. Sci.*, **77**, 1575–1582, https://doi.org/10.1175/JAS-D-19-0281.1.

Frierson, D. M. W., 2007a: Convectively coupled Kelvin waves in an idealized moist general circulation model. *J. Atmos. Sci.*, **64**, 2076–2090, https://doi.org/10.1175/JAS3945.1.

——, 2007b: The dynamics of idealized convection schemes and their effect on the zonally averaged tropical circulation. *J. Atmos. Sci.*, **64**, 1959–1976, https://doi.org/10.1175/JAS3935.1.

——, I. M. Held, and P. Zurita-Gotor, 2006: A gray-radiation aquaplanet moist GCM. Part I: Static stability and eddy scale. *J. Atmos. Sci.*, **63**, 2548–2566, https://doi.org/10.1175/JAS3753.1.

——, ——, and ——, 2007: A gray-radiation aquaplanet moist GCM. Part II: Energy transports in altered climates. *J. Atmos. Sci.*, **64**, 1680–1693, https://doi.org/10.1175/JAS3913.1.

Fuchs, Ž., and D. J. Raymond, 2002: Large-scale modes of a nonrotating atmosphere with water vapor and cloud–radiation feedbacks. *J. Atmos. Sci.*, **59**, 1669–1679, https://doi.org/10.1175/1520-0469(2002)059<1669:LSMOAN>2.0.CO;2.

——, and ——, 2005: Large-scale modes in a rotating atmosphere with radiative–convective instability and WISHE. *J. Atmos. Sci.*, **62**, 4084–4094, https://doi.org/10.1175/JAS3582.1.

——, and ——, 2017: A simple model of intraseasonal oscillations. *J. Adv. Model. Earth Syst.*, **9**, 1195–1211, https://doi.org/10.1002/2017MS000963.

Fuchs-Stone, Ž., and K. Emanuel, 2022: Sensitivity of linear models of the Madden–Julian Oscillation to convective representation. *J. Atmos. Sci.*, **79**, 1575–1584, https://doi.org/10.1175/JAS-D-21-0165.1.

Gill, A. E., 1980: Some simple solutions for heat-induced tropical circulation. *Quart. J. Roy. Meteor. Soc.*, **106**, 447–462, https://doi.org/10.1002/qj.49710644905.

Hannah, W. M., and E. D. Maloney, 2014: The moist static energy budget in NCAR CAM5 hindcasts during DYNAMO. *J. Adv. Model. Earth Syst.*, **6**, 420–440, https://doi.org/10.1002/2013MS000272.

Hu, Q., and D. A. Randall, 1994: Low-frequency oscillations in radiative-convective systems. *J. Atmos. Sci.*, **51**, 1089–1099, https://doi.org/10.1175/1520-0469(1994)051<1089:LFOIRC>2.0.CO;2.

Inoue, K., and L. E. Back, 2015a: Column-integrated moist static energy budget analysis on various time scales during TOGA COARE. *J. Atmos. Sci.*, **72**, 1856–1871, https://doi.org/10.1175/JAS-D-14-0249.1.

——, and ——, 2015b: Gross moist stability assessment during TOGA COARE: Various interpretations of gross moist stability. *J. Atmos. Sci.*, **72**, 4148–4166, https://doi.org/10.1175/JAS-D-15-0092.1.

——, and ——, 2017: Gross moist stability analysis: Assessment of satellite-based products in the GMS plane. *J. Atmos. Sci.*, **74**, 1819–1837, https://doi.org/10.1175/JAS-D-16-0218.1.

Jiang, X., and Coauthors, 2020: Fifty years of research on the Madden–Julian oscillation: Recent progress, challenges, and perspectives. *J. Geophys. Res. Atmos.*, **125**, e2019JD030911, https://doi.org/10.1029/2019JD030911.

Jucker, M., and E. P. Gerber, 2017: Untangling the annual cycle of the tropical tropopause layer with an idealized moist model. *J. Climate*, **30**, 7339–7358, https://doi.org/10.1175/JCLI-D-17-0127.1.

Khairoutdinov, M. F., and K. Emanuel, 2018: Intraseasonal variability in a cloud-permitting near-global equatorial aquaplanet model. *J. Atmos. Sci.*, **75**, 4337–4355, https://doi.org/10.1175/JAS-D-18-0152.1.

Kiladis, G. N., M. C. Wheeler, P. T. Haertel, K. H. Straub, and P. E. Roundy, 2009: Convectively coupled equatorial waves. *Rev. Geophys.*, **47**, RG2003, https://doi.org/10.1029/2008RG000266.

Kim, D., A. H. Sobel, and I.-S. Kang, 2011: A mechanism denial study on the Madden–Julian oscillation. *J. Adv. Model. Earth Syst.*, **3**, M12007, https://doi.org/10.1029/2011MS000081.

——, M.-S. Ahn, I.-S. Kang, and A. D. Del Genio, 2015: Role of longwave cloud–radiation feedback in the simulation of the Madden–Julian oscillation. *J. Climate*, **28**, 6979–6994, https://doi.org/10.1175/JCLI-D-14-00767.1.

Kiranmayi, L., and E. D. Maloney, 2011: Intraseasonal moist static energy budget in reanalysis data. *J. Geophys. Res.*, **116**, D21117, https://doi.org/10.1029/2011JD016031.

Klingaman, N. P., and S. J. Woolnough, 2014a: The role of air–sea coupling in the simulation of the Madden–Julian oscillation in the Hadley Centre model. *Quart. J. Roy. Meteor. Soc.*, **140**, 2272–2286, https://doi.org/10.1002/qj.2295.

——, and ——, 2014b: Using a case-study approach to improve the Madden–Julian oscillation in the Hadley Centre model. *Quart. J. Roy. Meteor. Soc.*, **140**, 2491–2505, https://doi.org/10.1002/qj.2314.

Kraucunas, I., and D. L. Hartmann, 2005: Equatorial superrotation and the factors controlling the zonal-mean zonal winds in the tropical upper troposphere. *J. Atmos. Sci.*, **62**, 371–389, https://doi.org/10.1175/JAS-3365.1.

Lutsko, N. J., 2018: The response of an idealized atmosphere to localized tropical heating: Superrotation and the breakdown of linear theory. *J. Atmos. Sci.*, **75**, 3–20, https://doi.org/10.1175/JAS-D-17-0192.1.

Madden, R. A., and P. R. Julian, 1971: Detection of a 40–50 day oscillation in the zonal wind in the tropical Pacific. *J. Atmos. Sci.*, **28**, 702–708, https://doi.org/10.1175/1520-0469(1971)028<0702:DOADOI>2.0.CO;2.

——, and ——, 1972: Description of global-scale circulation cells in the tropics with a 40–50 day period. *J. Atmos. Sci.*, **29**, 1109–1123, https://doi.org/10.1175/1520-0469(1972)029<1109:DOGSCC>2.0.CO;2.

——, and ——, 1994: Observations of the 40–50-day tropical oscillation—A review. *Mon. Wea. Rev.*, **122**, 814–837, https://doi.org/10.1175/1520-0493(1994)122<0814:OOTDTO>2.0.CO;2.

Majda, A. J., and S. N. Stechmann, 2009: The skeleton of tropical intraseasonal oscillations. *Proc. Natl. Acad. Sci. USA*, **106**, 8417–8422, https://doi.org/10.1073/pnas.0903367106.

——, and ——, 2011: Nonlinear dynamics and regional variations in the MJO skeleton. *J. Atmos. Sci.*, **68**, 3053–3071, https://doi.org/10.1175/JAS-D-11-053.1.

Maloney, E. D., and D. L. Hartmann, 1998: Frictional moisture convergence in a composite life cycle of the Madden–Julian oscillation. *J. Climate*, **11**, 2387–2403, https://doi.org/10.1175/1520-0442(1998)011<2387:FMCIAC>2.0.CO;2.

——, and A. H. Sobel, 2004: Surface fluxes and ocean coupling in the tropical intraseasonal oscillation. *J. Climate*, **17**, 4368–4386, https://doi.org/10.1175/JCLI-3212.1.

——, ——, and W. M. Hannah, 2010: Intraseasonal variability in an aquaplanet general circulation model. *J. Adv. Model. Earth Syst.*, **2** (2), https://doi.org/10.3894/JAMES.2010.2.5.

Matsuno, T., 1966: Quasi-geostrophic motions in the equatorial area. *J. Meteor. Soc. Japan*, **44**, 25–43, https://doi.org/10.2151/jmsj1965.44.1_25.

Merlis, T. M., T. Schneider, S. Bordoni, and I. Eisenman, 2013: Hadley circulation response to orbital precession. Part I: Aquaplanets. *J. Climate*, **26**, 740–753, https://doi.org/10.1175/JCLI-D-11-00716.1.

Nakazawa, T., 1988: Tropical super clusters within intraseasonal variations over the western Pacific. *J. Meteor. Soc. Japan*, **66**, 823–839, https://doi.org/10.2151/jmsj1965.66.6_823.

Neelin, J. D., I. M. Held, and K. H. Cook, 1987: Evaporation–wind feedback and low-frequency variability in the tropical atmosphere. *J. Atmos. Sci.*, **44**, 2341–2348, https://doi.org/10.1175/1520-0469(1987)044<2341:EWFALF>2.0.CO;2.

O'Gorman, P. A., and T. Schneider, 2008: The hydrological cycle over a wide range of climates simulated with an idealized GCM. *J. Climate*, **21**, 3815–3832, https://doi.org/10.1175/2007JCLI2065.1.

Paynter, D., and V. Ramaswamy, 2014: Investigating the impact of the shortwave water vapor continuum upon climate simulations using GFDL global models. *J. Geophys. Res. Atmos.*, **119**, 10 720–10 737, https://doi.org/10.1002/2014JD021881.

Ray, P., and C. Zhang, 2010: A case study of the mechanics of extratropical influence on the initiation of the Madden–Julian oscillation. *J. Atmos. Sci.*, **67**, 515–528, https://doi.org/10.1175/2009JAS3059.1.

——, ——, J. Dudhia, and S. S. Chen, 2009: A numerical case study on the initiation of the Madden–Julian oscillation. *J. Atmos. Sci.*, **66**, 310–331, https://doi.org/10.1175/2008JAS2701.1.

Raymond, D. J., S. L. Sessions, A. H. Sobel, and Ž. Fuchs, 2009: The mechanics of gross moist stability. *J. Adv. Model. Earth Syst.*, **1** (3), https://doi.org/10.3894/JAMES.2009.1.9.

Rostami, M., and V. Zeitlin, 2019: Eastward-moving convection-enhanced modons in shallow water in the equatorial tangent plane. *Phys. Fluids*, **31**, 021701, https://doi.org/10.1063/1.5080415.

Saravanan, R., 1993: Equatorial superrotation and maintenance of the general circulation in two-level models. *J. Atmos. Sci.*, **50**, 1211–1227, https://doi.org/10.1175/1520-0469(1993)050<1211:ESAMOT>2.0.CO;2.

Showman, A. P., and L. M. Polvani, 2011: Equatorial superrotation on tidally locked exoplanets. *Astrophys. J.*, **738**, 71, https://doi.org/10.1088/0004-637X/738/1/71.

Sobel, A. H., and H. Gildor, 2003: A simple time-dependent model of SST hot spots. *J. Climate*, **16**, 3978–3992, https://doi.org/10.1175/1520-0442(2003)016<3978:ASTMOS>2.0.CO;2.

——, and E. Maloney, 2012: An idealized semi-empirical framework for modeling the Madden–Julian oscillation. *J. Atmos. Sci.*, **69**, 1691–1705, https://doi.org/10.1175/JAS-D-11-0118.1.

——, and ——, 2013: Moisture modes and the eastward propagation of the MJO. *J. Atmos. Sci.*, **70**, 187–192, https://doi.org/10.1175/JAS-D-12-0189.1.

——, J. Nilsson, and L. M. Polvani, 2001: The weak temperature gradient approximation and balanced tropical moisture waves. *J. Atmos. Sci.*, **58**, 3650–3665, https://doi.org/10.1175/1520-0469(2001)058<3650:TWTGAA>2.0.CO;2.

Straub, K. H., 2013: MJO initiation in the real-time multivariate MJO index. *J. Climate*, **26**, 1130–1151, https://doi.org/10.1175/JCLI-D-12-00074.1.

Suarez, M. J., and D. G. Duffy, 1992: Terrestrial superrotation: A bifurcation of the general circulation. *J. Atmos. Sci.*, **49**, 1541–1554, https://doi.org/10.1175/1520-0469(1992)049<1541:TSABOT>2.0.CO;2.

Thayer-Calder, K., and D. A. Randall, 2009: The role of convective moistening in the Madden–Julian oscillation. *J. Atmos. Sci.*, **66**, 3297–3312, https://doi.org/10.1175/2009JAS3081.1.

Waliser, D. E., K. M. Lau, and J.-H. Kim, 1999: The influence of coupled sea surface temperatures on the Madden–Julian oscillation: A model perturbation experiment. *J. Atmos. Sci.*, **56**, 333–358, https://doi.org/10.1175/1520-0469(1999)056<0333:TIOCSS>2.0.CO;2.

Wang, B., and H. Rui, 1990: Dynamics of the coupled moist Kelvin–Rossby wave on an equatorial β-plane. *J. Atmos. Sci.*,

47, 397–413, https://doi.org/10.1175/1520-0469(1990)047<0397:DOTCMK>2.0.CO;2.

——, and G. Chen, 2017: A general theoretical framework for understanding essential dynamics of Madden–Julian oscillation. *Climate Dyn.*, **49**, 2309–2328, https://doi.org/10.1007/s00382-016-3448-1.

——, F. Liu, and G. Chen, 2016: A trio-interaction theory for Madden–Julian oscillation. *Geosci. Lett.*, **3**, 34, https://doi.org/10.1186/s40562-016-0066-z.

Wang, W., and M. E. Schlesinger, 1999: The dependence on convection parameterization of the tropical intraseasonal oscillation simulated by the UIUC 11-layer atmospheric GCM. *J. Climate*, **12**, 1423–1457, https://doi.org/10.1175/1520-0442(1999)012<1423:TDOCPO>2.0.CO;2.

Wedi, N. P., and P. K. Smolarkiewicz, 2010: A nonlinear perspective on the dynamics of the MJO: Idealized large-eddy simulations. *J. Atmos. Sci.*, **67**, 1202–1217, https://doi.org/10.1175/2009JAS3160.1.

Welch, P., 1967: The use of fast Fourier transform for the estimation of power spectra: A method based on time averaging over short, modified periodograms. *IEEE Trans. Audio Electroacoust.*, **15**, 70–73, https://doi.org/10.1109/TAU.1967.1161901.

Wheeler, M. C., and G. N. Kiladis, 1999: Convectively coupled equatorial waves: Analysis of clouds and temperature in the wavenumber–frequency domain. *J. Atmos. Sci.*, **56**, 374–399, https://doi.org/10.1175/1520-0469(1999)056<0374:CCEWAO>2.0.CO;2.

——, and H. H. Hendon, 2004: An all-season real-time multivariate MJO index: Development of an index for monitoring and prediction. *Mon. Wea. Rev.*, **132**, 1917–1932, https://doi.org/10.1175/1520-0493(2004)132<1917:AARMMI>2.0.CO;2.

Wolding, B. O., and E. D. Maloney, 2015: Objective diagnostics and the Madden–Julian oscillation. Part II: Application to moist static energy and moisture budgets. *J. Climate*, **28**, 7786–7808, https://doi.org/10.1175/JCLI-D-14-00689.1.

Yanai, M., S. Esbensen, and J.-H. Chu, 1973: Determination of bulk properties of tropical cloud clusters from large-scale heat and moisture budgets. *J. Atmos. Sci.*, **30**, 611–627, https://doi.org/10.1175/1520-0469(1973)030<0611:DOBPOT>2.0.CO;2.

Yang, D., and A. P. Ingersoll, 2013: Triggered convection, gravity waves, and the MJO: A shallow-water model. *J. Atmos. Sci.*, **70**, 2476–2486, https://doi.org/10.1175/JAS-D-12-0255.1.

——, and ——, 2014: A theory of the MJO horizontal scale. *Geophys. Res. Lett.*, **41**, 1059–1064, https://doi.org/10.1002/2013GL058542.

Yano, J.-I., and J. J. Tribbia, 2017: Tropical atmospheric Madden–Julian oscillation: A strongly nonlinear free solitary Rossby wave? *J. Atmos. Sci.*, **74**, 3473–3489, https://doi.org/10.1175/JAS-D-16-0319.1.

Yasunaga, K., S. Yokoi, K. Inoue, and B. E. Mapes, 2019: Space–time spectral analysis of the moist static energy budget equation. *J. Climate*, **32**, 501–529, https://doi.org/10.1175/JCLI-D-18-0334.1.

Zhang, C., Á. F. Adames, B. Khouider, B. Wang, and D. Yang, 2020: Four theories of the Madden–Julian oscillation. *Rev. Geophys.*, **58**, e2019RG000685, https://doi.org/10.1029/2019RG000685.